

Article

Synthetic neutrino imaging of a microquasar

Theodoros Smponias ¹

¹ Directorate of Secondary Education of the Dodekanese, Rhodes, Greece

* Correspondence: t.smponias@hushmail.com

Abstract: Microquasar binary stellar systems emit electromagnetic radiation and high energy particles over a broad energy spectrum. But they are so far away, that it is hard to observe their details. A simulation then offers the link between relatively scarce observational data and the rich theoretical background. In this work, high energy particle emission, from simulated twin microquasar jets, is calculated in a unified manner. From the cascade of emission within an element of jet matter, to the dynamic and radiative whole jet model, the series of physical processes involved are integrated together. A program suite assembled around model data produces synthetic images and spectra, directly comparable to potential observations by contemporary arrays. The model is capable of describing a multitude of system geometries, incorporating increasing levels of realism, depending on the needs and on available computational resources. As an application, the modelling process is applied to a typical microquasar, which is synthetically observed from different angles using various imaging geometries. Furthermore, the resulting intensities are found to be comparable to the sensitivity of existing detectors. The combined background emission from a potential distribution of microquasars is also modelled.

Keywords: ISM: jets and outflows; stars: winds-outflows; stars: flare; radiation mechanisms: general; methods: numerical

0. Introduction

Microquasars (MQ) comprise a binary stellar system where a main sequence star orbits a compact object, either a neutron star or a black hole [1]. Matter from the star accretes onto the collapsed stellar remnant, resulting in the production of twin relativistic jets, pointing in opposite directions. Those jets emit over a broad spectrum, from radio to very high energy (VHE) γ -rays and neutrinos [2], [3], [4], [5], [6].

As mentioned in [2], apparent superluminal motion in certain MQ indicate the presence of bulk hadron flows in the jets. The assumption of equipartition [5], leads to high magnetic field estimates for the jet [7]. This, coupled with the fluid approximation for the jet matter, due to the presence of tangled magnetic fields [8] [9], allows the magneto-hydrodynamic (MHD) approximation for the jets. A toroidal magnetic field component may retain jet collimation over considerable distances along its path [7] [10]. Moreover, external confinement from surrounding winds is equally important [11] [5].

In order to study the jets, a selection from among the wealth of theoretical results is compared to observations of those remote systems. The relative scarcity of detailed data is complemented by the use of numerical simulations of a jet system, where a model setup is evolved and then imaged synthetically. The final model emissions are placed next to observations, running many examples until a match is achieved. If no positive detections exist yet, then a general match to theoretical results and also to the sensitivity of active observing arrays is desired. As a next step, going backwards, the jet model is reverse-engineered to its initial, boundary and in general internal/unobservable conditions, which emerge as the link between jet theory and observations.

The above process is able to offer increased insight into the inner physical workings of the jets and their surroundings, allowing their study as a complex, evolving dynamical system. A more accurate description of the system of interest is then obtained.

Citation: Smponias, T Imaging of a microquasar. *Journal Not Specified* 2021, 1, 0. <https://doi.org/>

Received:

Accepted:

Published:

Publisher's Note: MDPI stays neutral with regard to jurisdictional claims in published maps and institutional affiliations.

Copyright: © 2021 by the authors. Submitted to *Journal Not Specified* for possible open access publication under the terms and conditions of the Creative Commons Attribution (CC BY) license (<https://creativecommons.org/licenses/by/4.0/>).

In this paper, the production of very high energy (VHE) neutrinos from generic MQ jets is modelled, using the method of dynamic and radiative relativistic MHD simulation. A set of surrounding winds assists with the confinement of the jets, adding realism to the model.

Within the jets, a complex, turbulent environment allows for the production of a variety of different signals, from radio to X and γ -rays. Furthermore, cascades of high energy particles produced in the jets, lead to an ecosystem of different particle populations, connected through transport phenomena. The production of neutrinos that leave the system, opens the possibility of detection at Earth, from modern arrays.

The solution of the transport equation from one particle distribution to the next, along a cascade, allows the expression of the intensity of emitted neutrinos, as a function of dynamic and radiative jet parameters at a given point. This way, local model parameters at each space-time point in the model jet are directly connected to the final particle emission at the same point. Repeating the latter process for a number of energies, provides a neutrino energy spectrum at each jet space-time point. Line of sight integration follows, leading to the production of a synthetic neutrino image of the system, and a whole-jet neutrino energy spectrum.

The paper is organized as follows: In Section 1 the theoretical background of the work is presented. In Section 2 the emission of particles from the jet is obtained. In Section 3 the results are presented and discussed. The normalization/equipartition (and the synthetic imaging process) are described in the Appendix.

1. Theoretical setup

In our generic MQ model, an accretion disk is assumed around the compact object [12]. Twin jets emanate from the vicinity of the collapsed star, collimated by a toroidal magnetic field component. Adopting a heavier pair of jets, their kinetic power is set to $L_k=2 \times 10^{38}$ (see Appendix). [5] argue a 10 percent Eddington luminosity jet power, leading to $L_k=10^{38} \text{ ergs}^{-1}$ for a $10 M_\odot$ black hole, which is comparable to our simulation. Furthermore, the same authors argue either $\frac{L_p}{L_e} \simeq 100$ or $\simeq 1$, and in our case we shall adopt the former hypothesis, favouring protons. As a first implementation, we shall calculate neutrino emission originating from the influence of the high-energy proton distribution, while there is also a potential comparable contribution from the corresponding high-energy electron distribution [5].

In the jets, equipartition is assumed between kinetic and magnetic energy densities, meaning $\rho_k = \rho_B$, therefore $B(z) = \sqrt{8\pi\rho_z}$ [8] [9], a close match with the B used in the simulation (see Appendix). External magnetic fields tend to be quite smaller [13], therefore, as a first-order approximation, they are not included in the surrounding winds.

1.1. Non-thermal proton density

Neutrino emission from the jets is taken to originate from proton-proton interaction between a distribution of hot (fast) protons and cold (bulk flow) protons [2,4–6,14,15]. Some of the bulk protons get accelerated at shock fronts, according to the first order Fermi acceleration mechanism, with a time scale of [16], [8], [9]

$$t_{\text{acc}}^{-1} \simeq \eta \frac{ceB}{E_p}, \quad (1)$$

where B is the magnetic field and E_p the proton energy, e being the proton charge and c the speed of light. $\eta = 0.1$ represents an acceleration efficiency parameter, assuming efficient acceleration in moderately relativistic shocks in the vicinity of the jet base [16].

As an approximation, the high-energy electron distribution is deferred to future work. Focusing on hadrons, we adopt a power-law distribution for the relativistic protons, of the form $N_p = N_0 E^{-\alpha}$ [11], with either $\alpha \approx 2$ [4], or a variable α [6], where α is the proton spectral index in the local jet cell matter frame. Alternatively, a transport equation could be used to find the distribution [4].

As a further approximation, the aforementioned hot proton distribution is taken to be isotropic in the jet frame, assuming the scattering length l_{sc} is less than the radiative length, l_r , a hypothesis backed by the nature of diffuse shock acceleration [17].

1.2. A note on jet frame anisotropy

For protons accelerated at diffuse shocks, the above assumption of isotropy is justified by the need to preserve, after every bounce, at least some proton energy [9]. Consequently, the scattering length l_{sc} is less than the radiative length l_r . Otherwise, the proton would not have any energy left after the bounce, negating the acceleration process.

According to [17], an assumed anisotropy of the hot proton distribution can be reflected to the neutrino distribution. In the jet system, emission would then be projected off axis, even reinforced, under certain orientations, in the lab frame.

2. Neutrino emission calculations

2.1. Proton energy loss

Following [14], [5], and [6], certain energy loss mechanisms are included. This presentation is performed at a cell with the properties of: $(u_x, u_y, u_z, b_x, b_y, b_z, n_p, \phi_1, \phi_2, \alpha) = (-0.3780c, 0.4480c, 0.0124c, 10^5G, 10^6G, 10^5G, 2.1 \times 10^{11} \text{ cm}^{-3}, 1.047 \text{ rad}, 5.00 \times 10^{-7} \text{ rad}, 2.0)$. As an exception, Figure 5 uses a different velocity vector, of $(0.2, 0.8, 0.1)c$. Nevertheless, in the model runs these are potentially performed in every cell.

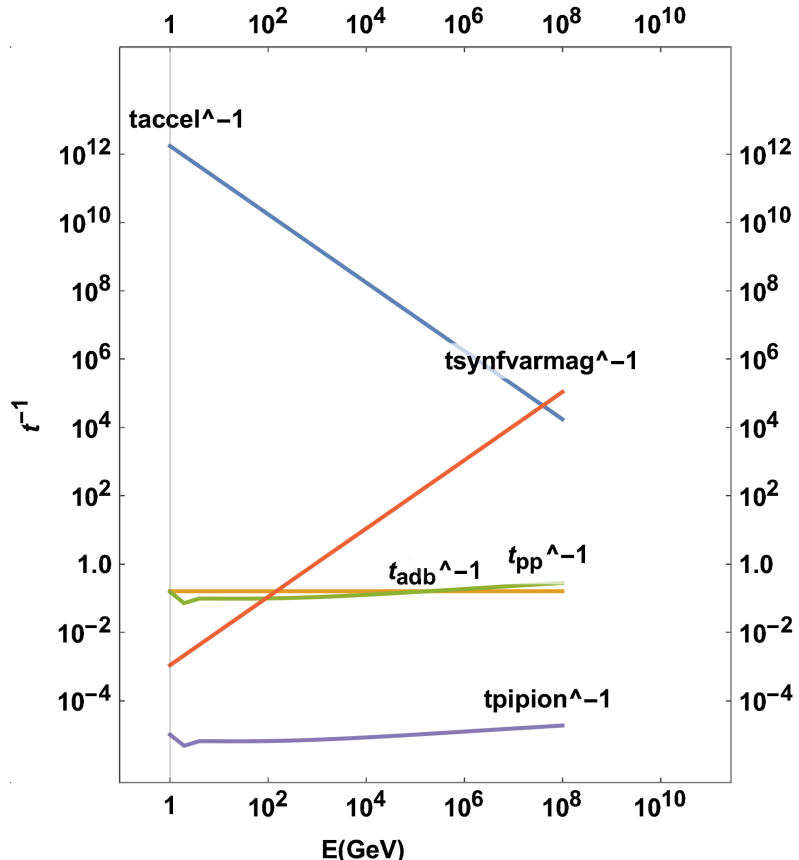


Figure 1. High energy proton distribution loss time scales, for various processes in the jets, plotted with energy in erg. t_{piion} stands for the pion decay timescale t_π .

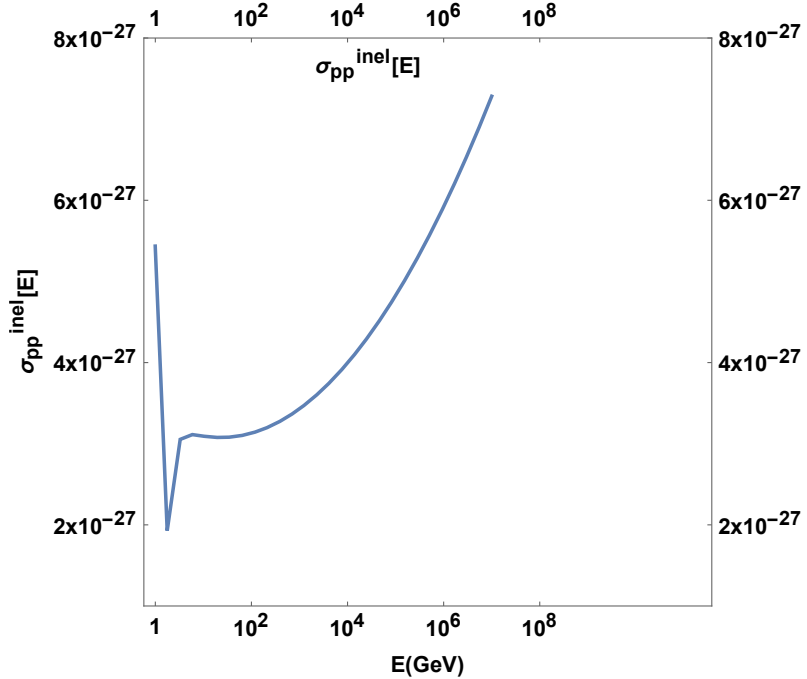


Figure 2. Inelastic proton-proton collision standard plotted with energy.

We consider a cutoff E for protons $E \leq 10^6$ GeV. For the adiabatic expansion time scale we have [5]

$$t_{\text{adb}}^{-1} = \frac{2}{3} \frac{u_b(\text{adb})}{z_j} \quad (2)$$

- 110 where $z_j = 10^{11}$ cm is the characteristic lateral size scale of the jet. For this simple calcula-
- 111 tion, $u_b(\text{adb})$ is preset to 0.8.

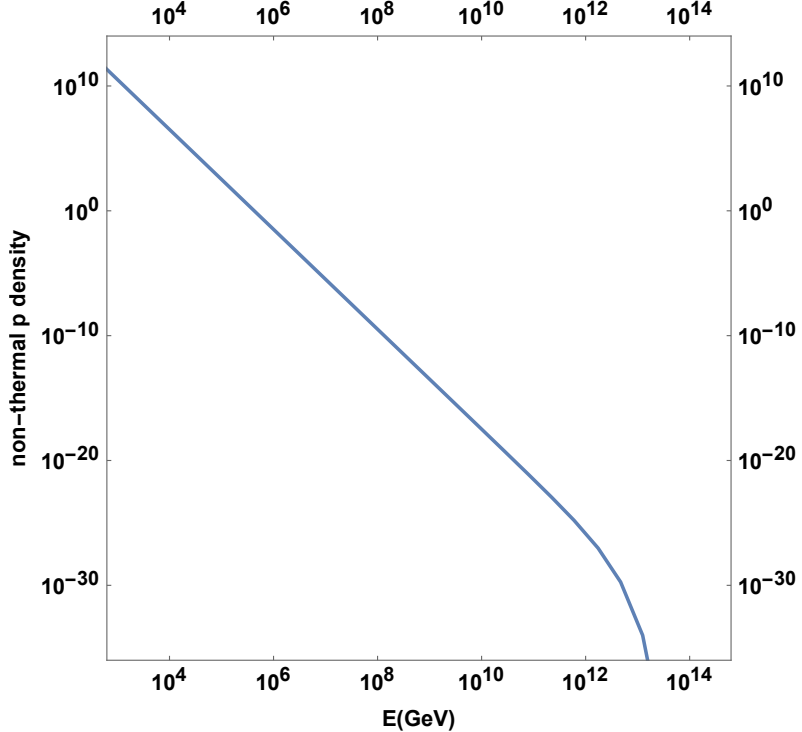


Figure 3. The density of non-thermal protons in the jet, using a high-energy cutoff feature, is plotted with energy.

For the p-p collision loss mechanism, we have

$$t_{pp}^{-1} = n c \sigma_{\text{inel}}(E_p) K_{pp} \quad (3)$$

$$\sigma_{pp}^{(\text{inel})} = (34.3 + 1.88L + 0.25L^2) \times [1 - (\frac{E_{th}}{E_p})^4]^2 \times 10^{-27} \text{ cm}^2 \quad (4)$$

¹¹² $\sigma_{pp}^{\text{inel}}$ is the inelastic p-p scattering cross section.
For the pion decay time we have

$$t_{\pi 0} = 2.6 \times 10^{-8} \text{ s} \quad (5)$$

and

$$t_\pi = t_{\pi 0} \Gamma_\pi + t_{\text{esc}} \quad (6)$$

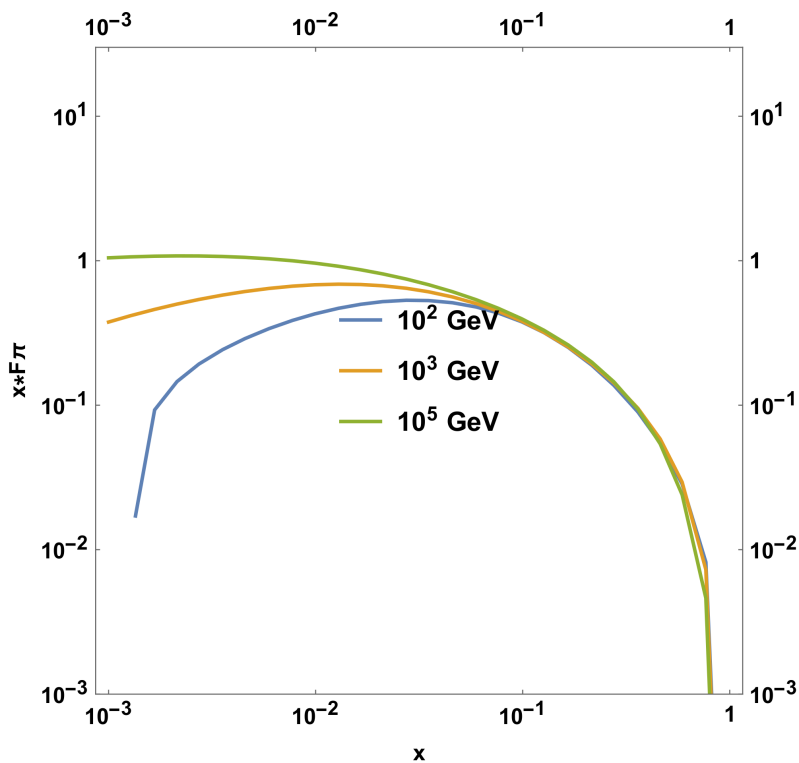


Figure 4. The F function, corresponding to the pion spectrum emerging from a single (hot-cold) proton collision, is presented here, multiplied by the $x = \frac{E_\pi}{E_p}$ fraction. The calculation is performed at three different energies for the non-thermal proton.

which in practice takes the form

$$t_\pi = t_{\pi 0} \left(\frac{E_\pi}{m_\pi c^2} \right) + t_{\text{esc}} \quad (7)$$

¹¹³ where the light escape time t_{esc} strongly affects the final result.

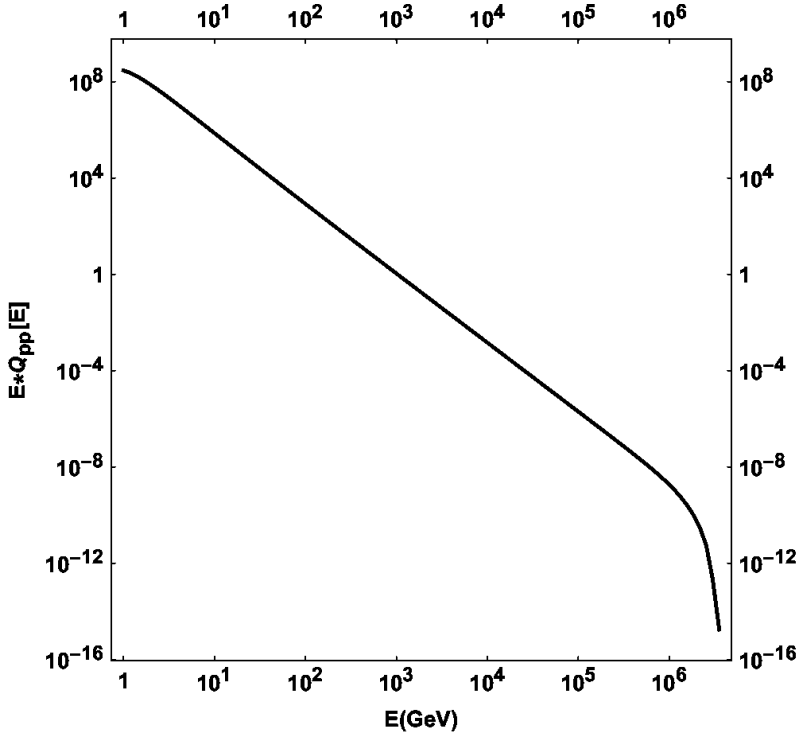


Figure 5. The pion injection function Q , weighted by pion energy, measured in non-normalized units, describing the combined spectrum from a multitude of (hot-cold) p-p collisions. We can see contributions rapidly declining as particle energy increases.

The synchrotron loss time scale is defined by

$$t_{\text{sync}}^{-1} = \frac{4}{3} \left(\frac{m_e}{m_p} \right)^3 \frac{1}{8\pi c m_e} \sigma_T B^2 \frac{E_p}{m_p c^2} \quad (8)$$

¹¹⁴ The form of the latter term, which is essentially Γ_p , facilitates energy-dependent calcula-
¹¹⁵ tions later-on. In total

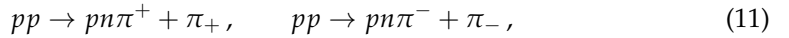
$$t_{\text{loss}}^{-1} = t_{\text{sync}}^{-1} + t_{\text{adb}}^{-1} + t_{pp}^{-1} \quad (9)$$

¹¹⁶ *2.2. A model for the interaction of thermal and non-thermal protons in the jet.*

Hot-cold proton interaction results to a distribution of high energy pions, which then decay allowing the creation of energetic neutrinos. We have [18–20]

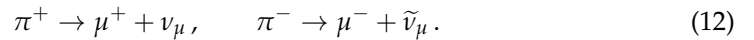


for neutral pions π^0 and



¹¹⁷ for π^\pm .

π^0 decay to gamma-rays, while π^\pm mostly to an anti-muon or muon and a muonic neutrino or anti-neutrino (prompt neutrinos) [18].



¹¹⁸ As an approximation, we neglect both neutrino production through secondary channels
¹¹⁹ and delayed neutrinos.

¹²⁰ For each successive particle population in the above cascades, the transport equation
¹²¹ [21] can be solved. Nevertheless, for protons a power-law distribution is assumed,

¹²² skipping having to solve the first transport equation in the cascade. From protons to
¹²³ pions then to muons and neutrinos, each generation of particles leads to the next one.
¹²⁴ [14] calculate the properties of resulting particle distributions over a large energy range,
¹²⁵ performing Monte Carlo calculations with the results of particle physics.

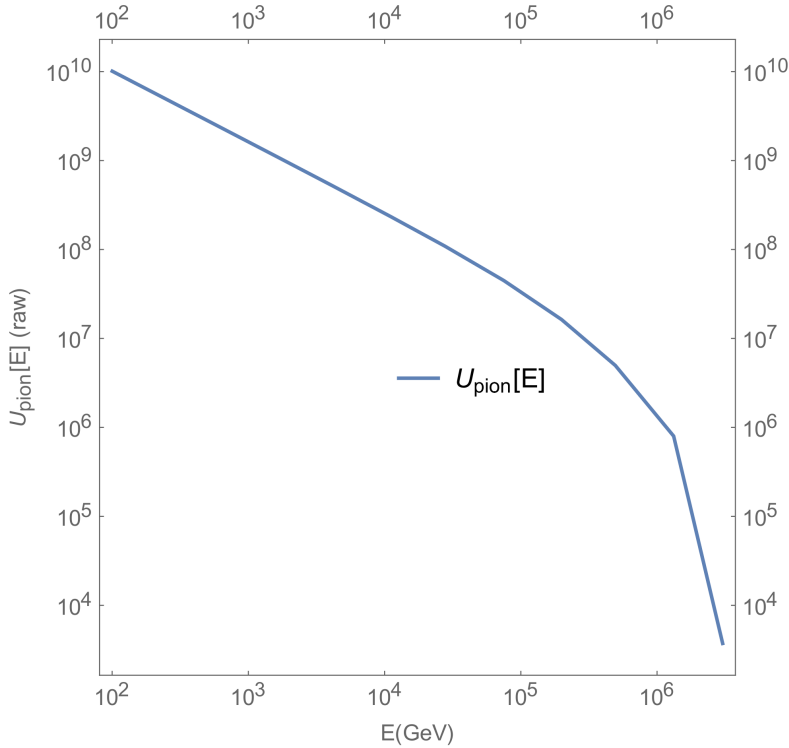


Figure 6. Pion energy distribution, plotted in non-normalized units versus energy.

¹²⁶ In previous works [20,22,23], the hadronic jet was modelled using the PLUTO code
¹²⁷ [24]. The results of PLUTO were then processed in order to calculate the emissivity of
¹²⁸ γ -rays and neutrino using various approximations. In this paper, the emissivity of
¹²⁹ neutrinos is calculated separately at each computational cell, using the angle (los, u),
¹³⁰ formed between the LOS and the local velocity.

¹³¹ PLUTO is an open-source, 2D/3D modular hydrocode, a finite-volume / finite-
¹³² difference, shock-capturing program, meant to integrate a set of (time-dependent) con-
¹³³ servation laws. Initial and boundary conditions are conveniently assigned through an
¹³⁴ equivalent set of primitive variables. The relevant systems of equations may include
¹³⁵ hydrodynamics (HD), magneto-hydrodynamics (MHD), and their special-relativistic
¹³⁶ counterparts, RHD and RMHD respectively, in either two or three spatial dimensions.
¹³⁷ The solution of conservation laws is carried out through discretization on a structured
¹³⁸ mesh, a logically rectangular grid, surrounded by a boundary, with additional ghost
¹³⁹ cells, in order to implement boundary conditions. The grid may either be static or
¹⁴⁰ adaptive, and various coordinate systems are available. The program may run efficiently
¹⁴¹ in parallel on various platforms.

¹⁴² 2.3. Lorentz transform of high E proton distribution

For the calculation of the fast proton distribution, the relevant directional equation is found in [25] [26]. The latest variant originates from [25] (TR), used here, minus a geometry factor that we absorb into the normalization factor

$$n(E, \theta) = \frac{\Gamma^{-\alpha-1} E^{-\alpha} (1 - \beta \cos(\theta) \sqrt{1 - \frac{m^2 c^4}{E^2}})^{-\alpha-1}}{[\sin^2(\theta) + \Gamma^2(\cos(\theta) - \frac{\beta}{\sqrt{1 - \frac{m^2 c^4}{E^2}}})^2]^{\frac{1}{2}}} \quad (13)$$

On the other hand, [26] (PS) say

$$n(E, \theta) = \frac{\Gamma^{-\alpha+1} E^{-\alpha} (1 - \beta \cos(\theta) \sqrt{1 - \frac{m^2 c^4}{E^2}})^{-\alpha}}{[\sin^2(\theta) + \Gamma^2(\cos(\theta) - \frac{\beta}{\sqrt{1 - \frac{m^2 c^4}{E^2}}})^2]^{\frac{1}{2}}} \quad (14)$$

And a simpler variant [22]

$$n(E, \theta) = \Gamma(E - \beta \sqrt{E^2 - m^2 c^4 \cos(\theta)}) \quad (15)$$

¹⁴³ The above are compared in Figures 7, 8 and 9.

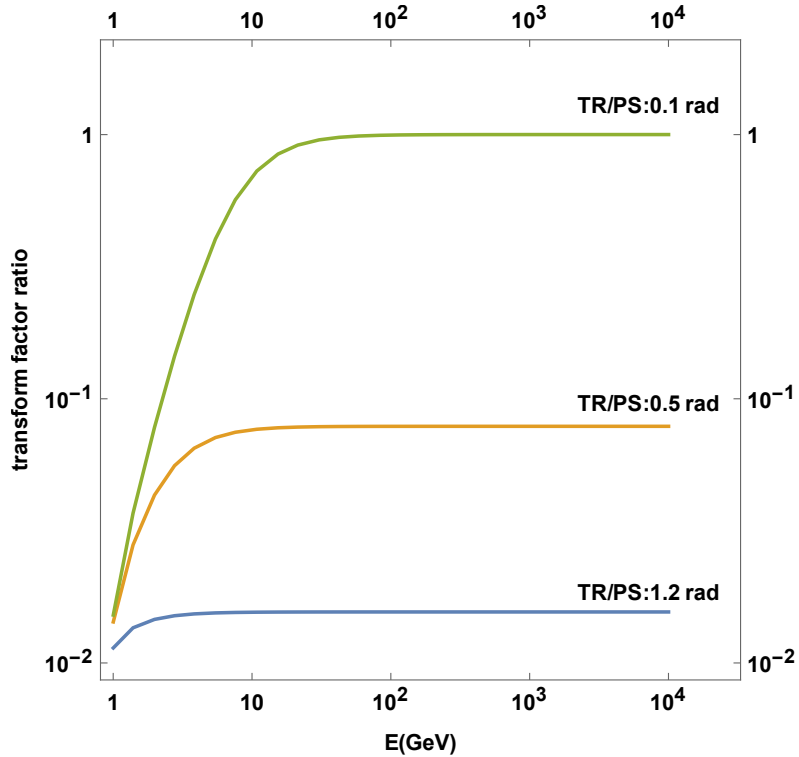


Figure 7. The ratio of high-energy proton distribution density transformation, for three different angles. A reproduction, for verification, of a figure from [25].

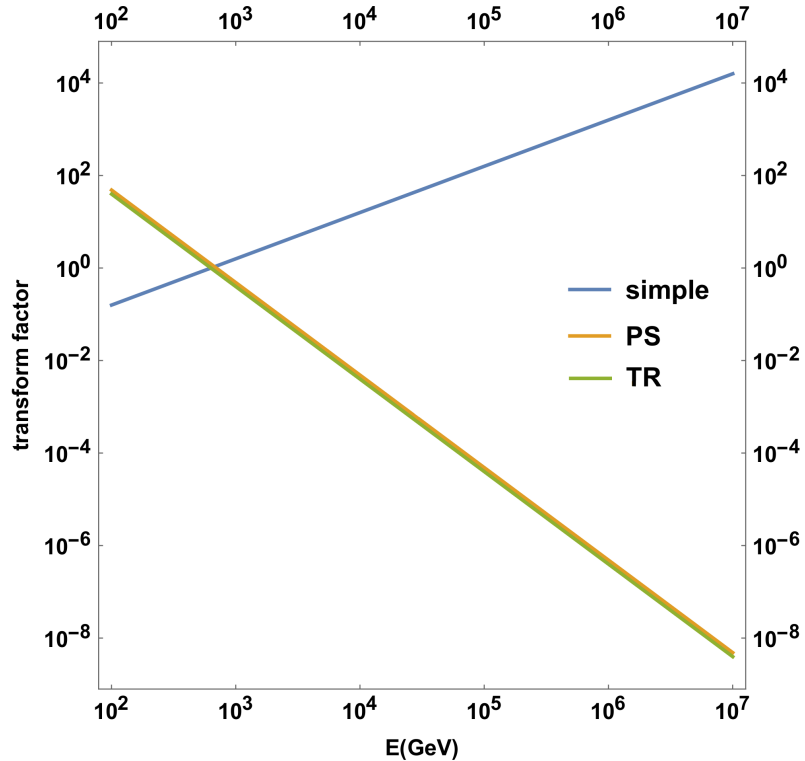


Figure 8. Three different expressions used for non-thermal proton distribution transform, plotted with energy.

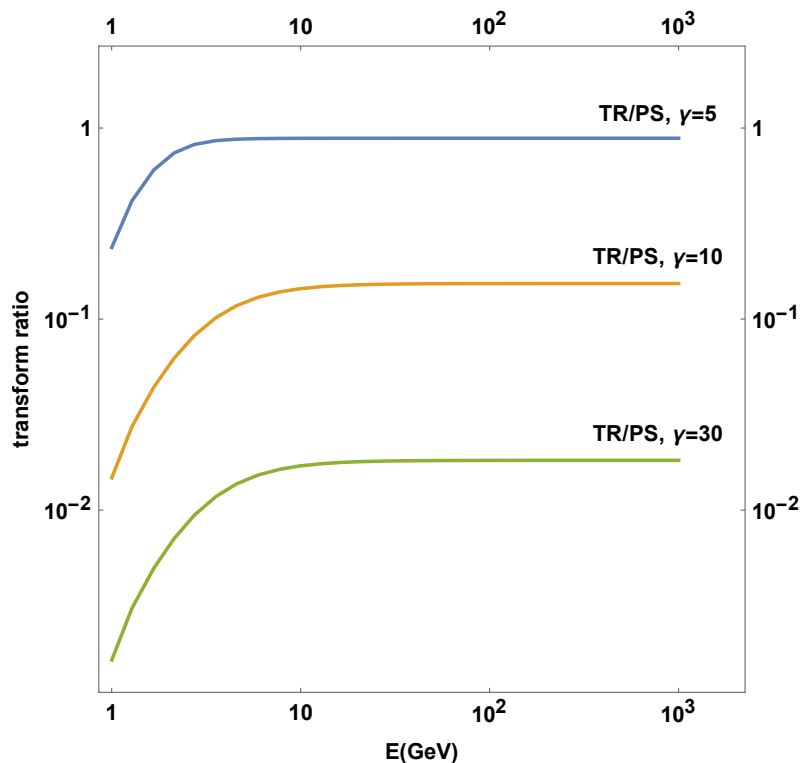


Figure 9. The ratio of TR/PS non-thermal proton distribution density transformation factors, for three different Lorentz factors. A reproduction, for verification, of a figure from [25].

¹⁴⁴ 2.4. Pion injection function and pion energy distribution

¹⁴⁵ For each fast-slow proton interaction a spectrum of possible pion energies exists,
¹⁴⁶ given by the function F_π ([14], [5] and [6]).

$$F_{\pi}^{(pp)}\left(x, \frac{E}{x}\right) = 4\alpha B_{\pi} x^{\alpha-1} \left(\frac{1-x^{\alpha}}{1+rx^{\alpha}(1-x^{\alpha})}\right)^4 \left(\frac{1}{1-x^{\alpha}} + \frac{r(1-2x^{\alpha})}{1+rx^{\alpha}(1-x^{\alpha})}\right) \left(1 - \frac{m_{\pi}c^2}{xE_p}\right)^{\frac{1}{2}} \quad (16)$$

¹⁴⁷ where $x = E/E_p$, and $L = \ln(E_p/1000\text{GeV})$, $E_{th} = 1.2 \text{ GeV}$ (see [5,14]).

¹⁴⁸ In Fig. 2 $\sigma_{pp}^{(\text{inel})}$ is plotted. In Fig. 3 the p-law fast proton density is shown. In Fig. 4
¹⁴⁹ $x F_{\pi}$ is plotted with the fraction x for different fast proton energies.

¹⁵⁰ The pion injection function, $Q_{\pi}^{(pp)}$, comprises, at each pion energy, pion contribu-
¹⁵¹ tions, to that pion energy, from the spectrum F , of all potential p-p interactions.

$$Q_{\pi}^{(pp)}(E, z) = n(z)c \int_{\frac{E}{E_p^{(\text{max})}}}^1 \frac{dx}{x} \left(\frac{E}{x}, z\right) F_{\pi}^{(pp)}\left(x, \frac{E}{x}\right) \sigma_{pp}^{(\text{inel})}\left(\frac{E}{x}\right), \quad (17)$$

¹⁵² x is the fraction of the pion energy to proton energy, and $n(z)$ is the jet flow proton
¹⁵³ density.

¹⁵⁴ In Fig 5 $Q_{\pi}^{(pp)}$ is plotted versus the pion energy E_{π} .

In order to obtain the pion distribution, we solve the following transport equation

$$\frac{\partial N_{\pi}}{\partial E} + \frac{N_{\pi}}{t_{\text{loss}}} = Q_{\pi}^{(pp)}(E, z) \quad (18)$$

¹⁵⁵ where $N_{\pi}(E, z)$ denotes the pion energy distribution. We proceed

$$N_{\pi}(E) = \frac{1}{|b_{\pi}(E)|} \int_E^{E^{(\text{max})}} dE' Q_{\pi}^{(pp)}(E') \exp[-\tau_{\pi}(E, E')], \quad (19)$$

¹⁵⁶ where

$$\tau_{\pi}(E', E) = \int_{E'}^E \frac{dE'' t_{\pi}^{-1}(E)}{|b_{\pi}(E'')|}. \quad (20)$$

¹⁵⁷ $b_{\pi}(E) = -E(t_{\text{sync}}^{-1} + t_{\text{adb}}^{-1} + t_{\pi p}^{-1} + t_{\pi\gamma}^{-1})$ is the energy loss rate of the pion. As an approxi-
¹⁵⁸ mation, the last term in the latter expression is omitted.

¹⁵⁹ The above are performed for each computational cell, where quantities, for radiative
¹⁶⁰ purposes, are considered locally constant. A cell is macroscopically large, inasmuch only
¹⁶¹ the deterministic portion of the transport equation is employed, in turn rendering it
¹⁶² deterministic. Again we take the characteristic scale (mean free path) of the radiative
¹⁶³ interactions to be smaller than the cell size, leading to the containment of particle
¹⁶⁴ interactions within a given hydrocode cell. Furthermore, the time scale for the radiative
¹⁶⁵ interactions is taken to be smaller enough than the hydrocode's timestep, that the
¹⁶⁶ radiative interactions belong to a single timestep each time.

¹⁶⁷ 2.5. Neutrino emissivity

¹⁶⁸ The emissivity of prompt neutrinos [4,5,14,15], is

$$Q_{\pi \rightarrow \nu}(E) = \int_E^{E_{\text{max}}} dE_{\pi} t_{\pi}^{-1}(E_{\pi}) N_{\pi}(E_{\pi}) \frac{\Theta(1 - r_{\pi} - x)}{E_{\pi}(1 - r_{\pi})}, \quad (21)$$

¹⁶⁹ $x = E/E_{\pi}$ and t_{π} is the pion decay timescale. $\Theta(\chi)$ is the theta function [5,20].

170 Neutrino emissivity is calculated for each individual cell, using the cell's own angle
 171 to the LOS crossing that cell. The imaging process may either incorporate parallel LOS's
 172 or a focused beam, where each LOS follows a slightly different path to a common focal
 173 point [27]. A synthetic image of the model system is thus produced.

174 3. Results and discussion

175 The jet base is situated near the centre of a Cartesian grid. A continuous model jet,
 176 representing a microquasar system, injected at $u_{jet} = 0.865c$ is studied with the RMHD
 177 setup of the PLUTO hydrocode, at a uniform grid resolution of $60 \times 100 \times 50$. The grid
 178 size is $(120 \times 10^{10} \text{ cm}) \times (200 \times 10^{10} \text{ cm}) \times (100 \times 10^{10} \text{ cm})$, therefore the cell length is
 179 $2 \times 10^{10} \text{ cm}$. In all of the model runs the same initial jet density of $10^{10} \text{ protons/cm}^3$
 180 is used, 2000 times less than the maximum surrounding gas density. Winds comprise
 181 an accretion disk wind construct and a stellar wind, which falls off away from the
 182 companion star, located off-grid at $(4 \times 10^{12} \text{ cm}, 1 \times 10^{12} \text{ cm}, 4 \times 10^{12} \text{ cm})$, while the jet
 183 is threaded by a strong confining toroidal magnetic field of $B=10^4 \text{ G}$. The simulations
 184 were run until $t = 842 \text{ s}$, saving a data snapshot every 25 (simulation) s. A snapshot of
 185 density is shown in Figures 10 and 11, in 3D and 2D respectively, where we can see the
 186 magnetically collimated jet pair advancing through surrounding winds.

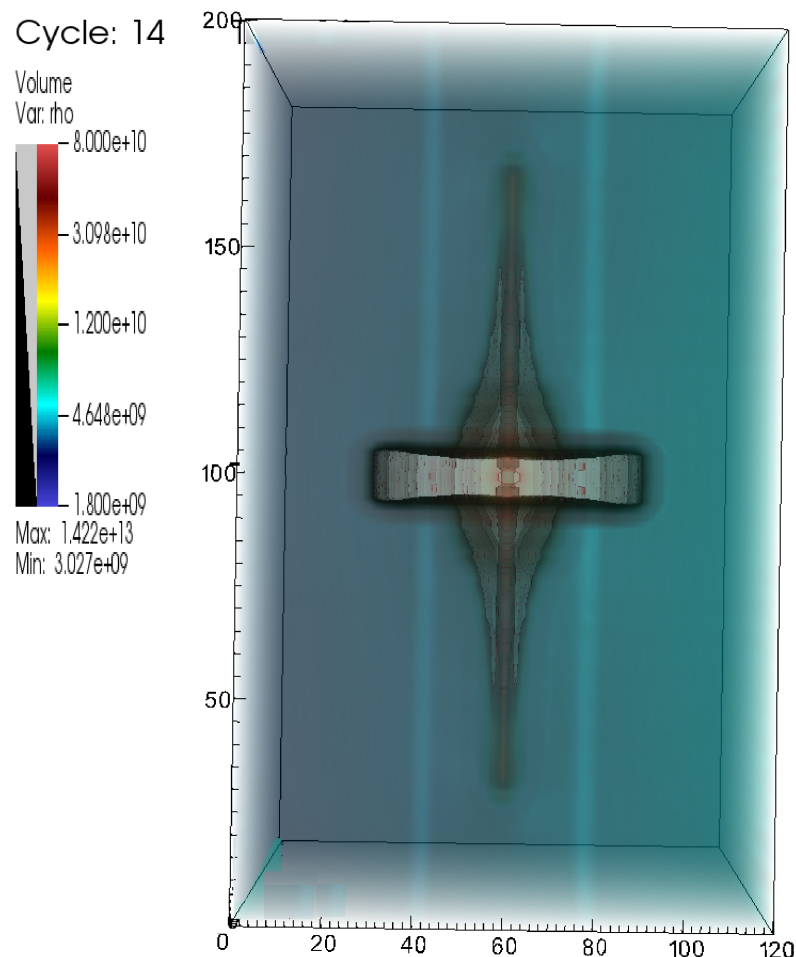


Figure 10. A three-dimensional view, from the side, of the twin model jet system. Snapshot 14 of the $u=0.866c$ hydrocode run, corresponding to a model time of $t=350 \text{ s}$ (14×25), depicting the density in a logarithmic plot. We can see both jet fronts advancing towards the ends of the grid, traversing the surrounding stellar wind, after crossing the simplified accretion disk wind construct. Image produced with VisIt.

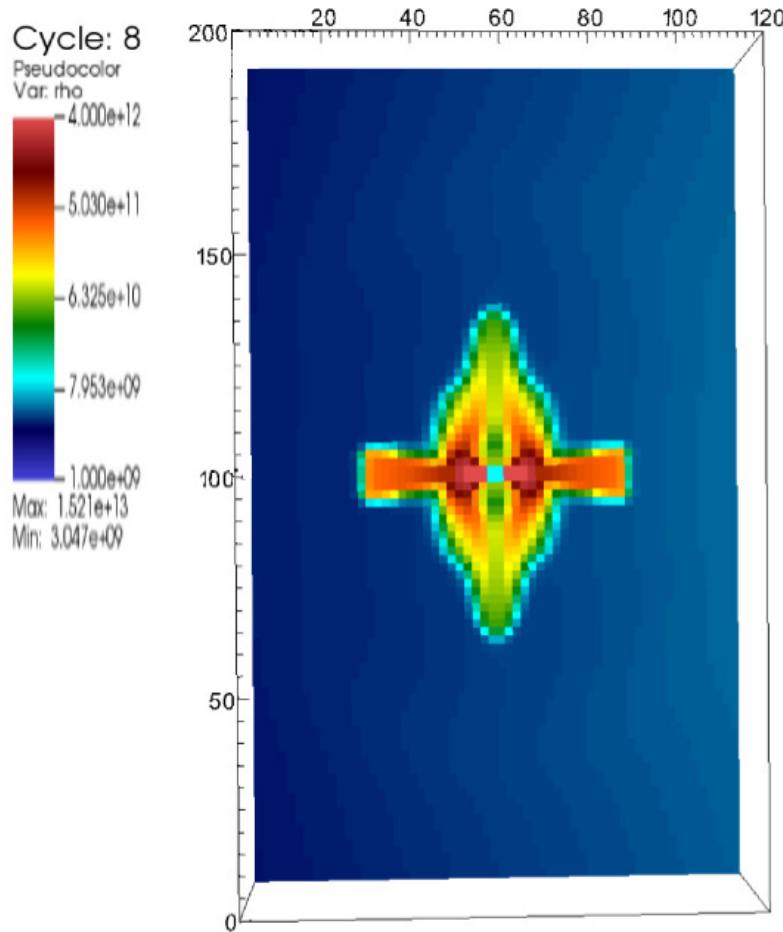


Figure 11. A two-dimensional slice view of the model system. More specifically, we can see snapshot 8 of the $u=0.866c$ hydrocode run, corresponding to a model time of $t=200$ s (8×25), depicting a slice of the density in a logarithmic plot, cut parallel to the jet axis. We can see both jet fronts traversing the stellar wind of the companion, after emerging from the model disk wind. Image produced with VisIt.

187 A number of empty user parameters were employed, in order to house particle
 188 emission results later on. Then, the above PLUTO run was copied into many directories.
 189 In each one of them, the nemiss program [28] was run, that calculates neutrino emission
 190 for a specific imaging geometry and setup. The results were overwritten into the suitably
 191 prepared data files of the originally empty user parameters of the hydrocode.

192 A series of imaging geometries were employed: No 1 means parallel rays, projected
 193 onto the XZ plane, no 2 the same but onto the YZ plane, no 3 is focused rays, onto the
 194 XZ plane, and no 4 is focused rays onto the YZ plane, see also Table 1. Three different
 195 angles were employed for the cases 1 and 2, while for cases 3 and 4 the respective focal
 196 points imply near-head-on and sidereal views.

197 Rlos2 [27] was then run, using the combined PLUTO-nemiss data, with sfactor=1
 198 for the pload shrink factor. In general, the imaging process may or may not use all
 199 snapshots available to it, depending on the light crossing time of its model segment
 200 (adjusted through the clight parameter in rlos2). Trying to read more snapshots than
 201 loaded corrupts the hydrocode time array of rlos2, called T, resulting to errors. For
 202 simplicity, in our case an artificially very high clight was used, in order to effectively
 203 switch off the time-delay effect. A double filter was used for velocity and for los,u angle.
 204 A minimum velocity and a maximum angle were set, in order to trigger the calculation of
 205 the neutrino emission for a particular cell. This way, the expensive part of the simulation

Viewing Angle	0 deg	10 deg	30 deg	60 deg	$\simeq 90$ deg	Comments
$l_{\text{cell}} (\times 10^{10} \text{ cm})$	2.0	2.0	2.0	2.0	2.0	PLUTO cell
$\rho_{\text{jet}} (\text{cm}^{-3})$	1.0×10^{10}	Jet's matter density				
$\rho_w (\text{cm}^{-3})$	1.0×10^{13}	Max wind density				
$\rho_{dw} (\text{cm}^{-3})$	2.0×10^{13}	Max disk wind density				
$t_{\text{run}}^{\max} (\text{s})$	842	842	842	842	842	Model run time
Method	P. L.	Piecewise Linear				
Integrator	M. H.	MUSCL-Hancock				
EOS	Ideal	Ideal	Ideal	Ideal	Ideal	Equation of state
BinSep (cm)	4.0×10^{12}	Binary separation				
M_{BH}/M_{\odot}	3-10	3-10	3-10	3-10	3-10	VE compact star mass
M_{\star}/M_{\odot}	10-30	10-30	10-30	10-30	10-30	Companion mass
$\beta = v_0/c$	0.866	0.866	0.866	0.866	0.866	Initial jet speed
L_k^p	2.5×10^{38}	Jet kinetic luminosity				
Grid resolution	$60 \times 100 \times 50$	PLUTO grid size (xyz)				
Imaging method	FB	PR	PR	PR	FB	Focused beam/parallel rays
Time delay	off	off	off	off	off	Very high LOS speed
Imaging plane	XZ-screen	XZ/YZ	XZ/YZ	XZ/YZ	YZ-screen	Box side or inner screen

Table 1: The five different imaging runs based on the same underlying hydrocode run are presented here.

206 was only performed where it was really worth it. This alleviated in part the discrepancy
 207 between computational costs of the dynamic and the radiative parts of the model.

208 An important aspect of this modelling approach is that each cell has a different
 209 emissivity visible from Earth, than its neighbors. That is because each cell may differ
 210 from the next one in terms of both speed and orientation to us. This combination means
 211 that, in general, the hydro model gives different results than the steady-state one. A
 212 vortex with relativistic velocities, for example, may in part appear very luminous, where
 213 it is fast with local speed pointing towards us, and also too dark, where velocities point
 214 away from us. In this simulation, such effects were limited, but at a higher resolution, it
 215 is expected than non-linear dynamic effects in the hydrocode shall interact profoundly
 216 with the radiative part of the model.

217 The scale of the total emission increases the closer the LOS gets to the jet pair axis
 218 Figures 12 and 13. The low resolution employed did not allow for significant non-linear
 219 dynamic effects to appear, yet the concept of the modelling process was proven to work
 220 in its entirety. On the other hand, the normalization process demonstrates the possibility
 221 of potential observations, as the results potentially fall within the detection range of
 222 contemporary arrays [5].

223 More specifically, we can see in the Appendix that the intensity at Earth is propor-
 224 tional to the kinetic jet luminosity L_k and also inversely proportional to the square of the
 225 distance to us D^2 . Consequently, a sample set of rates can be extracted from the model,
 226 and then used as a reference for other microquasars, at different distances and with
 227 different jet energies than the standard. In Figure 14 the weighted set of rates expected
 228 at Earth are presented, for a sample microquasar, viewed at 30 degrees from the jet axis,
 229 with $L_k=10^{38} \text{ ergs}^{-1}$ and $D=5 \text{ kpc}$. Other systems will then have $I = I_{0,\theta} \frac{L_k}{L_{k0}} \left(\frac{D_0}{D} \right)^2$, where
 230 I , L_k and D refer to a new microquasar, I_0 , L_{k0} and D_0 represent the standard plotted
 231 here, and the profound effect of the viewing angle is included in an implicit manner.

232 The result of Figure 14 is comparable to the sensitivity of IceCube in terms of a squared
233 energy weighted curve, which falls below 10^{-8} throughout the plot's energy span [29].

234 The above estimate may then be employed in order to provide a rough estimate of
235 expected neutrino emission from a distribution of microquasars in the galaxy. [30] argue
236 an estimated population of around a hundred systems in our galaxy. Furthermore, their
237 discussion of γ -ray emission from microquasars clarifies the importance of relativistic
238 boosting in jet emission. Thus, orientation to Earth plays a major role here, and the
239 situation is similar for neutrino emission.

240 We proceed accepting 100 systems, at various distances, ranging from a minimum
241 of 1 kpc to a maximum of 30 kpc, with an average kinetic luminosity similar to our
242 model system. The linear dependence of emission on the latter quantity facilitates such
243 a simplification. A distance of 1 kpc commands a flux at Earth of 25 times more than
244 our model value, whereas a system situated at 30 kpc will have 36 times less. Finally, an
245 orientation of less than 60 degrees might have 1 order of magnitude less than our value,
246 but a jet system aimed towards us will perhaps have up to 100 times more visibility at
247 Earth, unless a very fast jet occurred. Consequently, the single most important factor is
248 orientation, followed by distance and lastly by jet kinetic power. The latter order allows
249 an estimate of perhaps 5 percent, or five systems with a very high relativistic boosting
250 towards us, a number of maybe 40 or 50 at angles above 45 degrees and finally maybe
251 50 at below 45 degrees. The first five will probably contribute the most on average,
252 and the ones viewed from the side will have the smaller effect. A possible system at a
253 smaller distance would of course dominate the distribution, but the possibility for such
254 an occurrence is questionable.

255 Based on the above discussion, we then accept a rough average for a neutrino
256 emitting galactic microquasar located at 15 kpc, with the kinetic luminosity of our model
257 (less affecting factor anyway) and oriented at 30 degrees from the line of sight, which
258 is the case used in Figure 14. The reason for having the average angle at less than 45
259 degrees is the higher contribution from systems aimed towards us. We then multiply our
260 single microquasar result by 100 (population size), divide it by 3^2 (distance) and leave
261 the jet power effect at unity. A rough first estimate could then be to multiply our single
262 system result, at 30 degrees from the jet axis, by a factor of ten, Figure 15, and then use it
263 for comparison with observations.

264 The above result may vary to either direction by possibly an order of magnitude,
265 subject to a more detailed statistical analysis. This is because there are similar systems
266 with higher or lower jet kinetic power, as well as systems with various individual
267 properties. Nevertheless, it seems possible that the detection of a background emission
268 from a potential distribution of microquasars in the Galaxy is within the realm of modern
269 detector arrays. This is also a consideration for the next generation of new or upgraded
270 arrays being planned today. On the other hand, a single X-Ray Binary system also
271 looks promising as a galactic source of high energy neutrinos. This is a potential target
272 for a particle sensor with increased angular accuracy. The variability of microquasars
273 within the human timescale, combined with their relative stability as a known point
274 source, offers a good target for observation, especially combined with sensors working
275 in electromagnetic spectra, such as radio, X-rays and γ -rays. In such a case, a neutrino
276 observation of a microquasar may form part of a multi-wavelength observation effort
277 aimed at the system of interest.

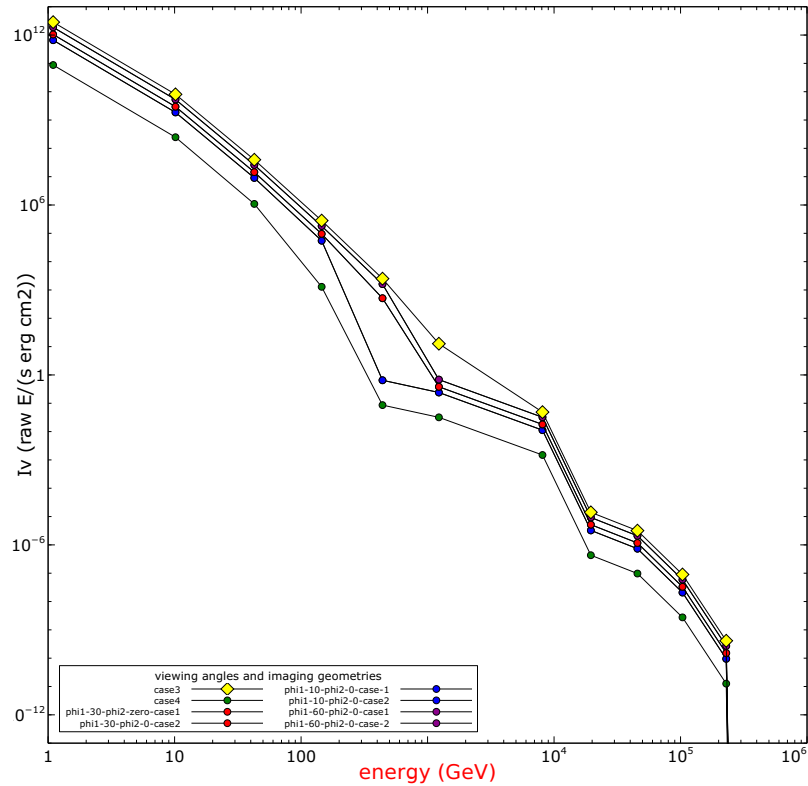


Figure 12. Non-normalized SED from a series of radiative simulations, based on the same RMHD dynamic model run. The plots are drawn using raw (arbitrary) units. The angle ϕ_1 is nearly 90 degrees when looking along the jet axis (imaging geometry case 3, focused beam) and zero when looking from the side (imaging geometry case 4, also focused beam). We can see the intensity dropping as the direction of observation deviates from the jet pair axis. Image produced with veusz, using data produced with PLUTO, rlos2 and nemiss.

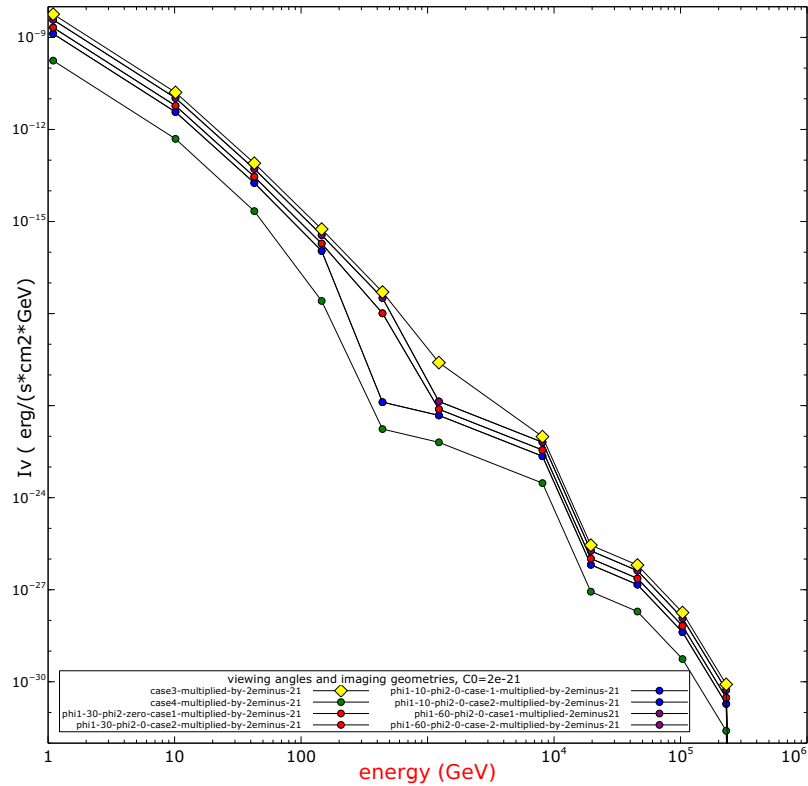


Figure 13. Normalized SED from a series of radiative simulations, where comparisons with potential observations are made possible. See the Appendix for more details on the normalization process. The angle $\phi_1 \simeq 90$ degrees in imaging geometry's case 3, and $\phi_1 \simeq 0$ in imaging geometry's case 4. The intensity decreases as the angle of observation moves away from the jet pair axis. Data finally processed and image produced with veusz.

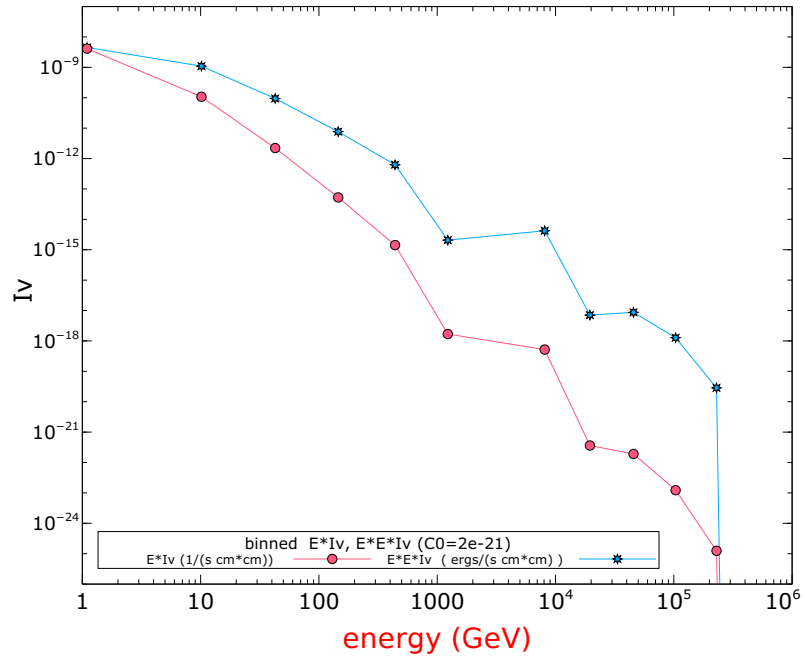


Figure 14. Intensity at Earth, at an angle $\phi_1 = 60$ degrees, meaning around 30 degrees from the jet axis, weighted by the energy/energy squared of the particle. These represent bin plots, since each data point lies on a higher size scale than the next one. Furthermore, they are also cumulative rate plots, upwards from each given energy, since rate contributions from higher energies are much smaller than the starter one. In comparison with the sensitivity of IceCube of below 10^{-8} in this plot, the results seem marginally acceptable in anticipation of potential detection. Image produced with veusz.

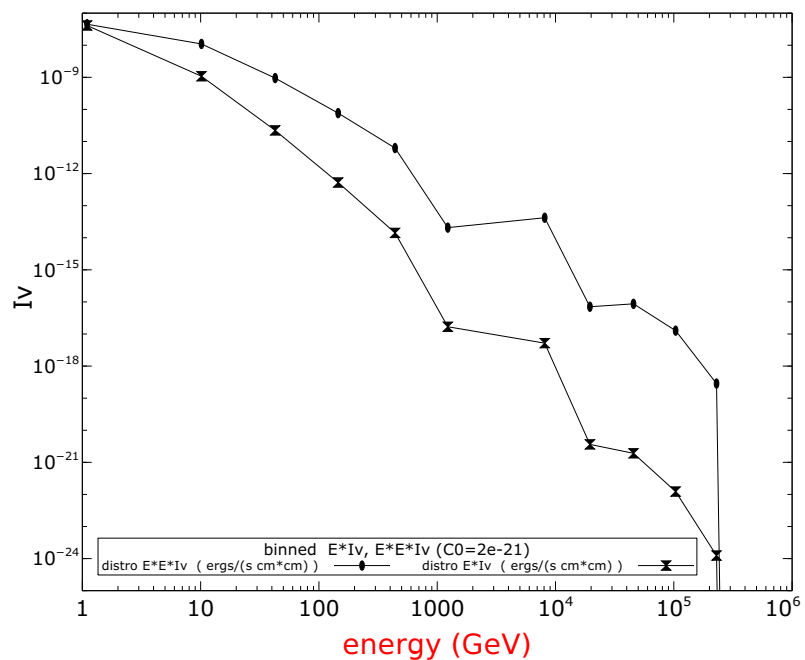


Figure 15. Intensity at Earth, of a fiducial distribution of systems, weighted by the energy/energy squared of the particle. Again, these may represent bin plots, due to the logarithmic decline of the quantity. For the same reason they are also cumulative rate plots, upwards from each given energy. Image produced with veusz.

278 4. Final remarks

279 Particle emission from a typical microquasar was simulated using a suitable pro-
280 gram suite. The results verified the integrity of the process, paving the way for more
281 detailed runs in the future. Furthermore, the model was employed in order to provide
282 particle emission estimates not only for a single microquasar, but also for a potential
283 galactic distribution of such systems. The latter approach facilitates comparison with
284 the output of contemporary detection arrays, where microquasars have the potential to
285 contribute to a background of high energy neutrinos.

286 In the model, a series of both dynamical and imaging parameters may be adjusted,
287 in order to cover different scenarios. The program suite works in a highly automated
288 manner, and is prepared to take on higher resolution applications, where the relativistic
289 effects of non-linear dynamics may appear in full.

290 The ability to focus on individual cells, has the potential to greatly differentiate each
291 jet element from the next one, in terms of emission. We can see that an MHD jet has great
292 local variability in both particle and radiation emission intensity in any given direction.
293 The detailed dynamics of the jet do influence the appearance of the system, depending
294 on both the direction and the magnitude of the local velocity, as well as on the pressure
295 and the density. Consequently, a jet system with turbulence, vortices, colliding with
296 clouds, etc, is expected to be subject to the aforementioned local variations of intensity.

297 As far as absorption is concerned, the model may directly include emission and
298 absorption of electromagnetic radiation, at different frequencies. Should adequate
299 computing resources be employed, the time-delayed description in the program can
300 also be activated. For example, a turbulent relativistic jet colliding with a cloud, has
301 different parts of it moving at high velocities, in different directions. The image is
302 then formed dynamically, the rays crossing a choreography of relativistically moving jet
303 elements. The final image may be quite different than initially expected, as demonstrated
304 for example by the effect of apparent superluminal motion. For a complex jet system,
305 running the model at higher resolutions with the time-delay module, has the potential
306 to reveal many physical details, drawing a more realistic picture of the system.

307 In general, microquasars may locally emit at reinforced levels of intensity, due to
308 the combination of jet dynamics and relativistic projection. The reason can be internal jet
309 turbulence, or interaction with clouds and surrounding winds. For γ -rays and neutrinos,
310 such dynamic effects should occur in the vicinity of the jet base.

311 Acknowledgements

312 We thank Prof. R. E. Spencer (Jodrell Bank Observatory) for valuable comments on
313 the manuscript. Special thanks go to Prof. G. E. Romero (UNLP, IAR) for his suggestions
314 on improving the content of this work.

315

- 316 1. Mirabel, I.F.; Rodríguez, L.F. *Ann. Rev. Astron. Astrophys.* **1999**, *37*, 409.
- 317 2. Romero, G.E.; Torres, D.F.; Kaufman Bernadó, M.M.; Mirabel, I.F. Hadronic gamma-ray
318 emission from windy microquasars. *Astron. & Astrophys.* **2003**, *410*, L1–L4, [[arXiv:astro-ph/0309123](https://arxiv.org/abs/astro-ph/0309123)]. doi:10.1051/0004-6361:20031314-1.
- 319 3. Bednarek, W. TeV Neutrinos from Microquasars in Compact Massive Binaries. *Ap. J.* **2005**,
320 *631*, 466–470, [[arXiv:astro-ph/0505547](https://arxiv.org/abs/astro-ph/0505547)]. doi:10.1086/432411.
- 321 4. Reynoso, M.M.; Romero, G.E.; Christiansen, H.R. Production of gamma rays and neutrinos
322 in the dark jets of the microquasar SS433. *MNRAS* **2008**, *387*, 1745–1754, [[arXiv:astro-ph/0801.2903](https://arxiv.org/abs/astro-ph/0801.2903)]. doi:10.1111/j.1365-2966.2008.13364.x.
- 323 5. Reynoso, M.M.; Romero, G.E. Magnetic field effects on neutrino production in micro-
324 quasars. *Astron. & Astrophys.* **2009**, *493*, 1–11, [[arXiv:astro-ph/0811.1383](https://arxiv.org/abs/astro-ph/0811.1383)]. doi:10.1051/0004-
325 6361:200811004.
- 326 6. Reynoso, M.M.; Carulli, A.M. On the possibilities of high-energy neutrino production in
327 the jets of microquasar SS433 in light of new observational data. *Astroparticle Physics* **2019**,
328 *109*, 25–32, [[arXiv:astro-ph.HE/1902.03861](https://arxiv.org/abs/astro-ph.HE/1902.03861)]. doi:10.1016/j.astropartphys.2019.02.003.

- 331 7. Koessl, D.; Mueller, E.; Hillebrandt, W. Numerical simulations of axially symmetric magnetized jets. I - The influence of equipartition magnetic fields. II - Apparent field structure and
332 theoretical radio maps. III - Collimation of underexpanded jets by magnetic fields. *Astron. & Astrophys.* **1990**, *229*, 378–415.
- 333 8. Rieger, F.M.; Duffy, P. A Microscopic Analysis of Shear Acceleration. *Ap. J.* **2006**, *652*, 1044–
334 1049, [[arXiv:astro-ph/astro-ph/0610187](https://arxiv.org/abs/astro-ph/astro-ph/0610187)]. doi:10.1086/508056.
- 335 9. Rieger, F.M. An Introduction to Particle Acceleration in Shearing Flows. *Galaxies* **2019**, *7*, 78,
336 [[arXiv:astro-ph.HE/1909.07237](https://arxiv.org/abs/astro-ph.HE/1909.07237)]. doi:10.3390/galaxies7030078.
- 337 10. Singh2019MHD. Study of relativistic magnetized outflows with relativistic equation
338 of state. *Monthly Notices of the Royal Astronomical Society* **2019**, *488*, 5713–5727,
339 [<https://academic.oup.com/mnras/article-pdf/488/4/5713/29191239/stz2101.pdf>].
340 doi:10.1093/mnras/stz2101.
- 341 11. Hughes, P.A. In *Beams and Jets in Astrophysics*; Hughes., Ed.; Cambridge University Press,
342 1991.
- 343 12. Fabrika, S. The jets and supercritical accretion disk in SS433. *2004*, *12*, 1–152, [[arXiv:astro-ph/0603390](https://arxiv.org/abs/astro-ph/0603390)].
- 344 13. Kološ, M.; Tursunov, A.; Stuchlík, Z. Possible signature of the magnetic fields related to
345 quasi-periodic oscillations observed in microquasars. *The European Physical Journal C* **2017**,
346 *77*. doi:10.1140/epjc/s10052-017-5431-3.
- 347 14. Kelner, S.R.; Aharonian, F.A.; Bugayov, V.V. Energy spectra of gamma rays, electrons, and
348 neutrinos produced at proton-proton interactions in the very high energy regime. *Phys. Rev. D* **2006**, *74*, 034018,
349 [[arXiv:astro-ph/astro-ph/0606058](https://arxiv.org/abs/astro-ph/astro-ph/0606058)]. doi:10.1103/PhysRevD.74.034018.
- 350 15. Lipari, P.; Lusignoli, M.; Meloni, D. Flavor composition and energy spectrum of astrophysical
351 neutrinos. *Physical Review D* **2007**, *75*. doi:10.1103/physrevd.75.123005.
- 352 16. Begelman, M.C.; Blandford, R.D.; Rees, M.J. Massive black hole binaries in active galactic
353 nuclei. *Nature* **1980**, *287*, 307–309. doi:10.1038/287307a0.
- 354 17. Derishev, E.V.; Aharonian, F.A.; Kocharyan, V.V. High-energy emission from off-axis
355 relativistic jets. *High Energy Gamma-Ray Astronomy*; Aharonian, F.A.; Völk, H.J.; Horns, D.,
356 Eds., 2005, Vol. 745, *American Institute of Physics Conference Series*, pp. 510–515, [[arXiv:astro-ph/0501197](https://arxiv.org/abs/astro-ph/0501197)]. doi:10.1063/1.1878454.
- 357 18. Kosmas, O.; Smponias, T. Simulations of Gamma-ray emission from magnetized micro-
358 quasar jets. *arXiv e-prints* **2018**, p. arXiv:1808.00303, [[arXiv:astro-ph.HE/1808.00303](https://arxiv.org/abs/astro-ph.HE/1808.00303)].
- 359 19. Smponias, T.; Kosmas, O. *Advances in High Energy Physics* **2017**, 4962741.
- 360 20. Smponias, T.; Kosmas, O. *Advances in High Energy Physics* **2015**, 921757.
- 361 21. James J. Duderstadt, W.R.M. *Transport theory*; Wiley: New York, 1979.
- 362 22. Smponias, T.; Kosmas, T.S. *MNRAS* **2014**, *438*, 1014.
- 363 23. Smponias, T.; Kosmas, T.S. *MNRAS* **2011**, *412*, 1320.
- 364 24. Mignone, A.; Bodo, G.; Massaglia, S.; Matsakos, T.; Tesileanu, O.; Zanni, C.; Ferrari, A. *Ap. J. Supp.* **2007**, *170*, 228.
- 365 25. Torres, D.F.; Reimer, A. Hadronic beam models for quasars and microquasars. *Astron. &*
366 *Astrophys.* **2011**, *528*, L2, [[arXiv:astro-ph.HE/1102.0851](https://arxiv.org/abs/astro-ph.HE/1102.0851)]. doi:10.1051/0004-6361/201116488.
- 367 26. Purmohammad, D.; Samimi, J. On the hadronic beam model of TeV gamma-ray flares from
368 blazars. *Astron. & Astrophys.* **2001**, *371*, 61–67. doi:10.1051/0004-6361:20010308.
- 369 27. Smponias, T. RLOS: Time-resolved imaging of model astrophysical jets, 2018, [[1811.009](https://arxiv.org/abs/1811.009)].
- 370 28. Smponias, T. nemiss: neutrino imaging of model astrophysical jets, 2019.
- 371 29. Hoshina, K.; Hodges, J.; Hill, G. In *Diffuse high-energy neutrino searches in AMANDA-II and*
372 *IceCube*; University of Wisconsin AMANDA/IceCube Collaboration, 2007; pp. <https://user-web.icecube.wisc.edu/~hoshina/diffuse/talks/DiffuseICRC2007.pdf>.
- 373 30. Paredes, J.M.; Martí, J. Microquasars in the galaxy. *Contributions to Science* **2003**, *2*, 303–314.
- 374 31. Weiskopf, D. Dissertation. PhD thesis, Dissertation, der Eberhard-Karls-Universität zu
375 Tübingen, der Fakultat fur Physik, 2001.
- 376 32. Cawthorne, T.V. In *Beams and Jets in Astrophysics*; Hughes., Ed.; Cambridge University Press,
377 1991.
- 378 33. Sparks, W.B.; Fraix-Burnet, D.; Macchetto, F.; Owen, F.N. A counterjet in the elliptical galaxy
379 M87. *Nature* **1992**, *355*, 804.
- 380 34. Laing, R.; Bridle, A.H. Relativistic models and the jet velocity field in the radio galaxy 3C 31.
381 *Monthly Notices of the Royal Astronomical Society* **2002**, *336*, 328.
- 382 35. Hjellming, R.M.; Johnston, K.J. *ApJ* **1988**, *328*, 600.

389 5. Appendix 1

390 5.1. Normalization

391 The kinetic energy of the jet at its base can be expressed as

$$E_k = \frac{1}{2}(\Gamma m)u^2 \quad (22)$$

where u is the jet speed, and m the mass of a jet portion crossing the cross section of the jet there. Then, the jet kinetic power, is the kinetic energy traversing the cross section per unit time

$$P_k = dE_k/dt = \frac{1}{2}(\Gamma dm/dt)u^2 \quad (23)$$

where the speed is taken constant during an ejection episode (it is also set constant in the simulation described here). But

$$dm/dt = \rho dV/dt = \rho A dx/dt = \rho Au \quad (24)$$

where A is the jet base cross section area, also taken constant both in the simulation and here. Therefore

$$P_k = dE_k/dt = \frac{1}{2}(\Gamma \rho A)u^3 \quad (25)$$

or

$$P_k = dE_k/dt = \frac{1}{2}(\Gamma \rho N_{\text{cell}} L_{\text{cell}}^2)u^3 \quad (26)$$

where $A = N_{\text{cell}} L_{\text{cell}}^2$. L_{cell}^2 is the area of the side of length L_{cell} of a cubical computational cell, at the jet base, and N_{cell} is the number of such cells forming the jet base. We then express density as a function of proton number density N_p and proton mass m_p

$$\rho = N_p m_p. \quad (27)$$

392 Furthermore, we introduce a factor $\alpha = L_v/L_k$, representing the portion of jet power
393 emitted in neutrinos. A typical value is taken as 10^{-3} . We also set $u=\beta c$. A less than
394 unity, positive filtering factor f_f is employed, which accounts for not using all of the
395 jet cells, but only those with velocity orientation closer to the LOS and also with speed
396 above a given limit.

We then have

$$L_v = \alpha L_k = \alpha P_k = \alpha dE_k/dt = f_f \frac{1}{2} \alpha \Gamma (N_p m_p N_{\text{cell}} L_{\text{cell}}^2) \beta^3 c^3 \quad (28)$$

The intensity of the jet is then expressed as $I_v = L_v/4\pi D^2$, where D is the distance to Earth. Thus

$$I_v = f_f \frac{1}{4\pi D^2} \alpha \frac{1}{2} \Gamma (N_p m_p N_{\text{cell}} L_{\text{cell}}^2) \beta^3 c^3 \quad (29)$$

397 In our simulation, the jet beam travels at $\beta = \frac{u}{c} = 0.866$, with a density of 10^{10} protons/cm³.
398 L_{cell} is 10^{10} cm, while the number of cells comprising the beam, at its base, at this
399 resolution, is $N_{\text{cell}} \simeq 15$. $\Gamma=2$. The distance to Earth, is taken here with a typical value of
400 $D=5$ kpc, or approximately 2×10^{22} cm.

401 We then integrate the area under the curve of the arbitrary units plot, for the case
402 of nearly non-beamed data, at $\phi_1=10$ degrees. That case is supposed, for the purposes
403 of normalization, to be the one matching the orientation of the hypothetical system
404 in relation to Earth. We do a cumulative sum over the roughly ten points, admitting
405 a ten percent coverage per order of magnitude scale level. Thus, we find about 10^{11} ,
406 which means that our sum is ten times smaller, or approximately 10^{10} , in arbitrary units
407 (AU)*GeV. We replace an AU with a constant C_0 , so that $AU = C_0 \text{ erg}/(\text{s} \cdot \text{cm}^2)$.

We set $I_\nu = L_\nu / 4\pi D^2$ equal to the area under the plot, expressed in units of C_0 , in order to find the latter (normalization constant)

$$I_\nu = f_f \frac{1}{4\pi D^2} \alpha \frac{1}{2} (\Gamma(N_p m_p) N_{\text{cell}} L_{\text{cell}}^2) \beta^3 c^3 = (\text{PLOTAREA}) * C_0 \text{ erg}/(\text{s cm}^2) \text{ GeV} \quad (30)$$

⁴⁰⁸ For our case, we find $C_0 \simeq 2 * 10^{-21}$, which is the value of the arbitrary unit C_0 . Using
⁴⁰⁹ the above constant, we multiply by it the value given in arbitrary units for the particle
⁴¹⁰ emission. Thus the intensity plot is multiplied, and we arrive to the updated plot in
⁴¹¹ Figure 13, which may be directly compared to other models and to observations.

⁴¹² 6. Appendix 2

The equipartition calculation now follows. As shown above, the jet kinetic power is

$$\dot{L}_k = \frac{1}{2} \frac{dm}{dt} u^2 = \frac{1}{2} (\rho A u) u^2 = \frac{1}{2} \rho A u^3 \quad (31)$$

⁴¹³ where $\frac{dm}{dt} = \rho \frac{dV}{dt} = \rho A \frac{dx}{dt} = \rho A u$
The kinetic energy density is [5]

$$\rho_k = \frac{\dot{L}_k}{\pi R_j^2 u_j} = \frac{\dot{L}_k}{A u} = \frac{\frac{1}{2} \rho A u^3}{A u} = \frac{1}{2} \rho u^2 \quad (32)$$

⁴¹⁴ which also acts as verification.

We also have

$$B = \sqrt{8\pi\rho_B} \quad (33)$$

For equipartition, we set the kinetic and magnetic energy densities equal to each other, $\rho_k = \rho_B$. So

$$B = \sqrt{8\pi\rho_B} = \sqrt{8\pi\rho_k} \quad (34)$$

We can now have ρ_k and then we shall calculate the B that corresponds to equipartition for that. Our beam has $\rho = 10^{10} \text{ cm}^{-3}$, or about $1.6 \times 10^{-14} \text{ g cm}^{-3}$. So

$$\rho_k = \frac{1}{2} (1.6 \times 10^{-14} \frac{g}{cm^3}) (\frac{\sqrt{3}}{2} 3 \times 10^{10} \frac{cms^2}{}) \simeq 5.4 \times 10^6 \frac{g}{cms^2} \quad (35)$$

Therefore, in CGS

$$B = \sqrt{8\pi\rho_k} \simeq \sqrt{8\pi 5.4 \times 10^6} \simeq 11.5 \times 10^3 \quad (36)$$

⁴¹⁵ For our simulation we set a rounded value of $B = 10^4 \text{ G}$, which is not far from the
⁴¹⁶ approximate equipartition value found above.

⁴¹⁷

⁴¹⁸ 7. Appendix 3

⁴¹⁹ The RLOS special relativistic imaging program is described here.

⁴²⁰ 7.1. Relativistic Effects

⁴²¹ The main effects of the Lorentz/Poincaré transform on the emission from a rela-
⁴²² tivistic object [31], specifically applied to an astrophysical jet, are relativistic aberration,
⁴²³ time dilation and frequency shift [11,32–34].

⁴²⁴ 7.1.1. Lorentz factor

⁴²⁵ The Lorentz factor for a hydrocode cell is [11]

$$\Gamma_{\text{Lorentz}} = \frac{1}{\sqrt{1 - u^2}} \quad (37)$$

where

$$u = \sqrt{u_x^2 + u_y^2 + u_z^2} \leq 1 \quad (38)$$

⁴²⁶ is the value of the local velocity $\vec{u} = (u_x, u_y, u_z)$, in units of the speed of light.

⁴²⁷ 7.1.2. Doppler factor calculation

Jet radiation is either boosted or de-boosted, depending on the angle losu, between the direction of the LOS and \vec{u} . The higher the jet speed, the narrower and stronger the cell boost cones around the jet head direction. On the other hand, outside cell boost cones, de-boosting occurs, that is to say the higher the velocity is, the weaker the signal becomes. D equals

$$D = \frac{\sqrt{1 - u^2}}{(1 - u * \cos(\text{losu}))} \quad (39)$$

⁴²⁸ For both the above equations, the angle between the LOS and the local velocity
⁴²⁹ vector is required at every point of the computational space.

⁴³⁰ For particles, their distribution is transformed to the Earth frame, as shown in
⁴³¹ [25].

⁴³² The cosine of angle losu is calculated in the following manner:

Let us define a fiducial unitary LOS vector $(\vec{LOS}) = (lx_1, lx_2, lx_3)$, with $(LOS) = \sqrt{lx_1^2 + lx_2^2 + lx_3^2} = 1$. In the following, ϕ_1 and ϕ_2 represent azimuth and elevation angles 1 and 2, respectively.

$$lx_1 = \cos(\phi_1)\cos(\phi_2), \quad lx_2 = \sin(\phi_1)\cos(\phi_2), \quad lx_3 = \sin(\phi_2) \quad (40)$$

$$\widehat{LOS * \vec{u}} = (LOS) * u * \cos(\widehat{LOS, \vec{u}}) = \widehat{LOS * \vec{u}} = lx_1 * u_x + lx_2 * u_y + lx_3 * u_z \quad (41)$$

Therefore, we have $((LOS)=1)$

$$\cos(\widehat{LOS, \vec{u}}) = \frac{lx_1 * u_x + lx_2 * u_y + lx_3 * u_z}{(LOS) * u} = \frac{lx_1 * u_x + lx_2 * u_y + lx_3 * u_z}{\sqrt{(u_x^2 + u_y^2 + u_z^2)}} \quad (42)$$

⁴³³ A minuscule number is added to the denominator of equation 42, in case $u=0$. The
⁴³⁴ above calculation allows the assignment of a Doppler boosting factor, through equations
⁴³⁵ 38, 39 and 42, to each discrete emission event along a line of sight.

⁴³⁶ 7.1.3. Doppler boosting

⁴³⁷ This area refers to electromagnetic emissions, but not to particle emission.

The jet spectrum is given by any suitable form inserted into the model. Earth frame jet spectrum S_{obs} can be expressed [11,32] as

$$S_{obs} = S_{jet} D^{3+\alpha} \quad (43)$$

⁴³⁸ where α is the spectral index. The exponent $(3+\alpha)$ in the above can be broken down into
⁴³⁹ different contributions from separate effects. Two units come from the aberration of
⁴⁴⁰ light, one from the relativistic dilation of time and α from the effect of frequency shift,
⁴⁴¹ while for a continuous optically thin jet a D factor is lost [32].

⁴⁴² Aberration-searchlight effect

⁴⁴³ Relativistic aberration changes the perceived direction of light (there is no curving
⁴⁴⁴ in Special Relativity), when transforming between the jet frame and the earth frame,
⁴⁴⁵ 'tilting rays', emanating from the jet, generally towards its head area.

⁴⁴⁶ Cell emission along a ray *within* the cell's boost cone, is then reinforced accordingly,
⁴⁴⁷ while if *outside* the cone it is weakened. Depending on the local velocity value and
⁴⁴⁸ direction, successive or neighbouring cells may have totally different boost cones.

⁴⁴⁹ Time dilation

⁴⁵⁰ Time dilation contributes one D factor to the emission result. Again, this refers to
⁴⁵¹ E/M radiation.

⁴⁵² 7.2. 3-dimensional imaging

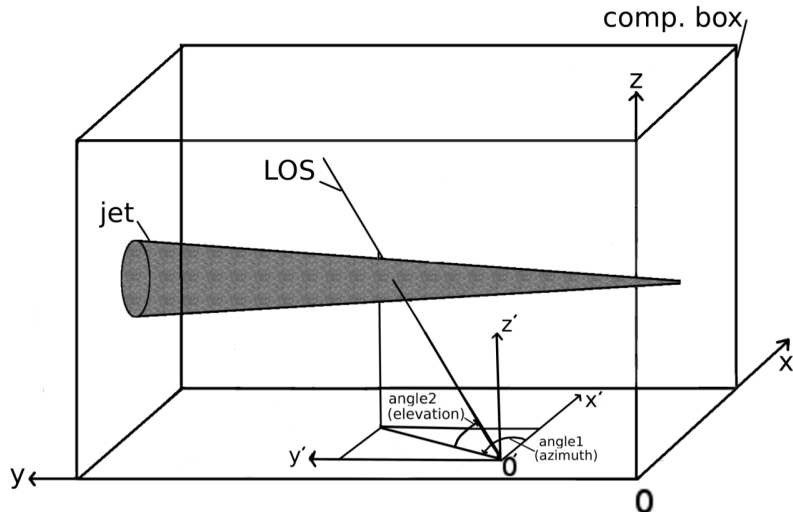


Figure 16. A 3D schematic view, of RLOS applied to a model astrophysical jet. The imaging side of the computational box is the yz plane, located on the side of the box apparently closer to the reader. Lying on the yz plane, O' is the point of origin of a random LOS, with its own dashed coordinate system $x'y'z'$. Alternatively, the imaging plane may also lie on the xz side of the box. The final image is taken to form on the eye or detector of a fiducial observer, situated at the end of the LOS.

⁴⁵³ The 3D setup of RLOS emulates that of its ancestor classical imaging code ([18,22,
⁴⁵⁴ 23]). From each pixel of the "imaging" side, of the 3D computational domain (Figure
⁴⁵⁵ 16), a line of sight (LOS) is drawn, through the imaged volume. Along the LOS, the
⁴⁵⁶ equation of radiative transfer is solved at each cell, using local emission and absorption
⁴⁵⁷ coefficients. Depending on the situation modelled, coefficients may either be calculated
⁴⁵⁸ directly, or outsourced to another program.

⁴⁵⁹ Lines of sight are drawn, starting from a pixel of the yz -side or xz -side (either
⁴⁶⁰ way called the imaging side) of the domain, tracing their way along the given direc-
⁴⁶¹ tion (Figures 16 and 17), until they reach a length of $\sqrt{(x_{max}^2 + y_{max}^2 + z_{max}^2)}$, where
⁴⁶² $x_{max}, y_{max}, z_{max}$ are the dimensions, in cells, of the computational domain. In practice,
⁴⁶³ on reaching the ends of the domain a LOS calculation halts, therefore some LOS's end
⁴⁶⁴ up shorter than others. The above process is repeated within a 2D loop, running over
⁴⁶⁵ the imaging plane, each LOS corresponding to a single pixel of the final synthetic image.
⁴⁶⁶ As an approximation, along a LOS no sideways scattering is considered.

⁴⁶⁷ A model astrophysical system may be inserted into RLOS directly, for example
⁴⁶⁸ forming a 'conical' jet setup [35]. Alternatively, data output from a hydrocode may be
⁴⁶⁹ employed, which is the case in the current paper, using PLUTO [24].

⁴⁷⁰ 7.3. Time-resolved imaging

⁴⁷¹ 7.3.1. Accessing 4-dimensional data

⁴⁷² The finite nature of the speed of light affects the appearance of a fast-moving object
⁴⁷³ in a crucial manner. Consequently, drawing a relativistic image of an astrophysical
⁴⁷⁴ system, necessitates the availability of information regarding not only its spatial prop-
⁴⁷⁵ erties, but its temporal evolution as well. In our case, when executing the hydrocode,
⁴⁷⁶ before running RLOS, we adjust the temporal density of snapshots, to be saved to disk

477 at regular intervals. The smaller those intervals, the better the temporal resolution of
 478 hydrocode data. A series of snapshots shall then be loaded to RAM by RLOS, which
 479 therefore requires a multiple quantity of memory, in order to run properly, than the
 480 hydrocode itself. Time is measured in simulation time units, which are read by PLUTO's
 481 attached 'pload.pro' routine, which loads data into RLOS.

482 The total time span available to a LOS, $\Delta t_{LOS(total)} = t_{(last-shot)} - t_{(first-shot)}$ ¹ (as
 483 measured in simulation time units, *not* merely in number of snapshots), should be preset
 484 to be larger than the light crossing time of the model system, at the selected LOS angle
 485 settings. Documenting the model jet evolution generally requires hydrocode data saves
 486 to be rather dense in time, especially for fast-changing flows. On the other hand, a lower
 487 temporal resolution will probably suffice for a steadier, slower-paced flow.

488 7.3.2. Traversing the 4D arrays

489 Introduction

490 A series of hydrocode snapshots are loaded to RAM, populating the elements of
 491 4-dimensional (4D) arrays. From a *temporal* point of view, we begin from the simulation
 492 time corresponding to the first of the loaded snapshots, called shotmin. From a *spatial*
 493 point of view, we start at the first point of the imaging plane, which is a side of the
 494 computational box (Figure 16). As the calculation advances, in 3D space, along the LOS
 495 being drawn (Figure 17), the algorithm keeps checking whether to jump to a new *temporal*
 496 slice, while staying 'on target' in 3D (Figure 18). Consequently, the LOS advances in
 497 time, through data (Figure 19), by accessing successive instants from the 4D data arrays.

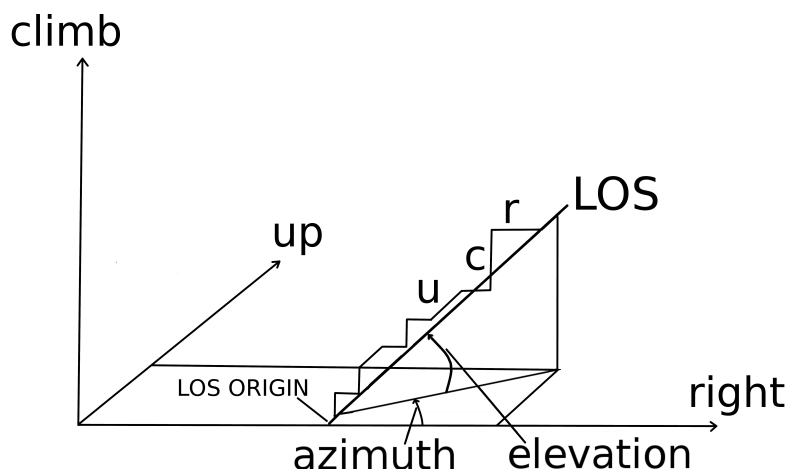


Figure 17. A schematic of the spatial propagation of the line of sight (LOS) through the 3D Cartesian computational grid. In the discrete grid, according to the design of the algorithm, there are 3 available directions to be taken at each step along the LOS: *right*, *up* and *climb*. These correspond to x, y and z, respectively. During propagation, the LOS 'tries' to follow its given direction, as defined by the two angles of azimuth and elevation. More specifically, every two steps a decision if first made on azimuth, either right or up. Then, for elevation, it is either climb, or another azimuth decision. In the Figure, along the LOS, horizontal steps point to the 'right' direction. Diagonal steps represent going 'up', while vertical ones constitute 'climb' steps.

498 Time-resolved imaging calculations

499 For every LOS, there is a point of origin (POO), located on the "imaging side" of the
 500 computational grid (Figure 16). That point, addressed in the code as (nx10, ny10, nz10)
 501 and here as O', is the beginning of the LOS's axes x', y', z', parallel to x, y, z respectively.

¹ Not to be confused with the interval Δt_{shot} between successive snapshots

⁵⁰² A 2D loop covers the imaging surface, the POO successively locating itself at each of the
⁵⁰³ latter's points.

⁵⁰⁴ As we progress along a LOS, a record is kept of where we are, in 3D space. This
⁵⁰⁵ record comprises the LOS's own integer coordinates, rc , uc , and cc , measured, in cells,
⁵⁰⁶ from its POO. The above symbols stand for right-current, up-current and climb-current,
⁵⁰⁷ representing the current LOS advance in the x' , y' and z' axes, respectively (Figures 16
⁵⁰⁸ and 17). The current ray position is then $(nx10+rc, ny10+uc, nz10+cc)$.

⁵⁰⁹ A timer variable, $curtime$ (standing for current LOS time), is introduced for each
⁵¹⁰ LOS, recording the duration of insofar ray travel along the LOS. The aforementioned
⁵¹¹ timer is preset at the beginning of each LOS, to the hydrocode time of the first loaded
⁵¹² data snapshot.

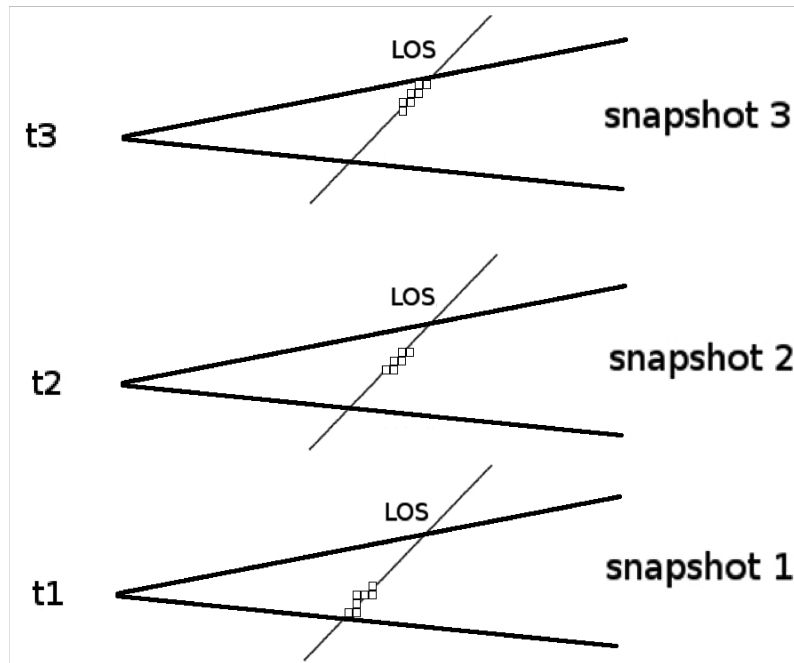


Figure 18. Three successive instants of a line of sight traversing a jet. At regular intervals, we jump to a new 3D slice of a 4D spacetime array, obtaining a discrete approximation of the time continuum, in the form of hydrocode snapshots.

⁵¹³ We then proceed to calculate the current length of the LOS

$$l_{los(current)} = [(dlr * (nx1current - nx10))^2 + (dlu * (ny1current - ny10))^2 + (dlc * (nz1current - nz10))^2]^{1/2} \quad (44)$$

where the LOS length is measured in cell length units and

$$nx1current = nx10 + rc, \quad ny1current = ny10 + uc, \quad nz1current = nz10 + cc \quad (45)$$

⁵¹⁴ Along the x , y and z directions, dlc , dlu , dlr are the respective *normalized* hydrocode
⁵¹⁵ cartesian cell lengths. Their values are usually unity, or close to unity, as set in the
⁵¹⁶ hydrocode by the user, and RLOS requires them fixed, meaning only homogeneous
⁵¹⁷ grids are currently supported. Furthermore, if the hydrocode grid is read, by pload, at a
⁵¹⁸ reduced resolution, then RLOS cell sizes are automatically adjusted accordingly.

We can finally write

$$l_{los(current)} = [((dlr * rc)^2) + ((dlu * uc)^2) + ((dlc * cc)^2)]^{1/2} \quad (46)$$

We then proceed to calculate curtime, the current hydro simulation time of the light ray along the LOS.

$$\text{curtime} = l_{\text{los}(\text{current})}/c_{\text{light}} + t_0(\text{LOS}). \quad (47)$$

519 $t_0(\text{LOS})$ is the timestamp of the first loaded snapshot, when the LOS begins to be drawn,
520 from its point of origin, and c_{light} is the speed of light, in cells per simulation second.

521 When curtime exceeds the next snapshot's timetag, the algorithm switches to
522 drawing the LOS through the 3D volume of the next available snapshot (Figure 18). We
523 keep moving along the same LOS in 3-D space, but we have just shifted to a new instant
524 in the time records of the hydrocode. The above temporal shift is repeated as many times
525 as required by the relevant criterion along the LOS, until the spatial end of the LOS.

526 7.3.3. Aiming the line of sight

527 The direction of a LOS in 3D space is defined by the two angles of azimuth (angle 1)
528 and elevation (angle 2) (Figure 16), where the plane of angle 1 is the $x'y'$ plane, parallel
529 to xy . For a jet parallel to the y axis, the angle between the local jet matter velocity \vec{u} , and
530 the LOS, $\text{losu} = (\widehat{\text{LOS}}, \vec{u})$, is usually small, when angle 1 approaches 90 degrees, and vice
531 versa (Figure 20). As is well known [11], the angle losu affects the relativistic emission
532 calculations.

533 Short of jet precession occurring, the plane of angle 2 (elevation) is largely perpendicular
534 to the jet when angle 1 is zero, while it is roughly parallel to the jet when angle 1 is
535 90 degrees. Usually, the jet bears an approximate cylindrical symmetry, meaning that for
536 a small angle 1, by varying angle 2, we 'rotate' the view around the jet axis, producing
537 similar intensities throughout the way. In summary, for a jet moving along the y axis,
538 the smaller angle 1 is, the less difference varying angle 2 makes.

539 On the other hand, for angle 1 nearing $\pi/2$, varying angle 2 rotates the view
540 within a plane approximately parallel to the jet, resulting to considerable differences.
541 Consequently, the larger angle 1 is, the stronger the effect, on the synthetic image, from
542 changing angle 2.

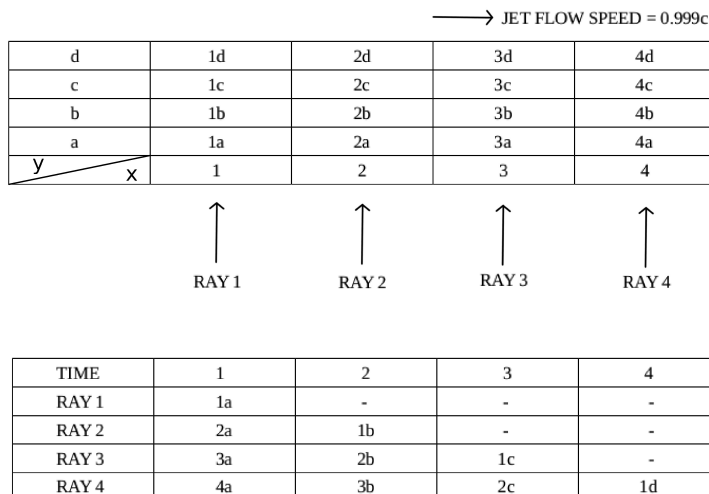


Figure 19. Simultaneous advance, in both space (2D) and time, of a few lines of sight. Top half depicts the spatial situation at $t=1$. Sixteen jet matter portions currently occupy this mini 4 by 4 grid. Each piece of matter is named after its position at $t=1$ and retains that name as it moves along. The bottom half shows how the situation evolves as time marches on, with light rays meeting different jet segments that cross their path. A dash means a light ray meeting jet matter other than the above, or nothing at all.

543 7.4. Frequency-shift

544 This area only refers to EM waves, not neutrinos.

Radiation emitted at a given frequency, from fast-moving jet matter, is taken to be Doppler shifted in frequency

$$f_{obs} = f_{calc}D \quad (48)$$

where f_{obs} is the observed frequency and f_{calc} is the frequency used in the emission calculations, performed in the jet frame of reference [11]. In order to accommodate for the shift, a power-law spectrum, falling off with frequency, is employed

$$S_{obs}(f) \propto f^{-\alpha} \quad (49)$$

⁵⁴⁵ with α assumed, as an approximation, to take the value of $\alpha = 2.0$, generally referring
⁵⁴⁶ to the optically thin region of the jet. For $D \geq 1$, emission is calculated at a frequency
⁵⁴⁷ lower than the observed, resulting to a higher intensity, since the spectrum employed
⁵⁴⁸ generally decreases with frequency.

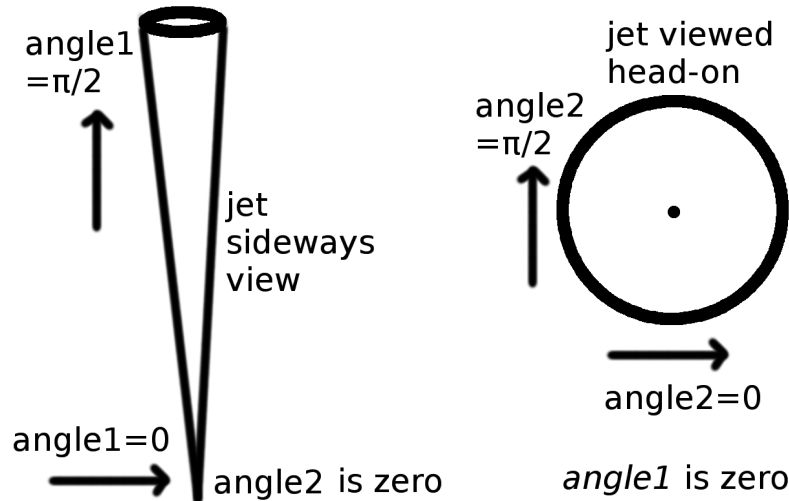


Figure 20. The geometric arrangement with regard to the viewing angles in the model, for the special cases of $angle2 = 0$ (left) and $angle1 = 0$ (right). For each sub-case, the arrow shows the direction of the LOS, which is different than the reader's direction of view.

⁵⁴⁹ Alternative frequency shift

⁵⁵⁰ RLOS may include different emission dependencies on frequency, where we calculate
⁵⁵¹ intensity at f_{calc} and observe that at f_{obs} .

⁵⁵² At the moment, the above is included only as a quantitative indicator, where
⁵⁵³ intensity may be optionally multiplied by the square of the ratio $f_{calc}/f_{obs} = 1/D^2$,
⁵⁵⁴ partially negating the effect of Doppler boosting.

⁵⁵⁵ **8. RLOS210**

⁵⁵⁶ RLOS version 2.10 was ready in November 2019. It includes a unified, function-
⁵⁵⁷ alized, modular approach. Both XZ and YZ versions have now been unified, for both
⁵⁵⁸ focused beam and also parallel LOS's. Code was re-organized and a series of tests are
⁵⁵⁹ included.

⁵⁶⁰ 0

⁵⁶¹ **8.1. RLOS210 commentary transcript**

⁵⁶² This is the latest version of rlos. Version 2 is a major upgrade of the original rlos
⁵⁶³ code. This time the program is broken up into procedures and functions, with a modular
⁵⁶⁴ structure.

⁵⁶⁵ The program allows the user to select which case to simulate, through an external
⁵⁶⁶ parameter file. There is a unified approach, where the same modules operate on different
⁵⁶⁷ geometries, through parameterization.

568 The user may select the values of the parameters of rlos version 1, and fully employ
569 them. As mentioned above, there is no more a different version of rlos for XZ and YZ
570 plane image formation. Now, there is one version of the code for both cases. Furthermore,
571 for each of those cases the user may select either radiograph or camera obscura imaging
572 technique.

573 Radiograph has all Lines of Sight parallel to each other, just like rlos v.1. This means
574 the film (fiducial imaging screen) is the size of the scene (grid), like an X-ray medical
575 image. The latter type of image shows clearly the various details of the system.

576 On the other hand, camera obscura, or focused beam, has a focal point, where the
577 eye of the fiducial observer is located. The imaging screen, in camera obscura, is also of
578 varied size: It may be equal, or smaller to the grid slice, at a given point along either x or
579 y axis, depending on YZ or XZ imaging plane case. At the moment, the fiducial imaging
580 screen must be parallel to the corresponding side of the grid, i.e. either XZ or YZ. Screen
581 location on-axis may vary within the grid. The smaller the screen, the smaller the image.

582 The focal point may reside either on the side of the grid, or outside the grid, but
583 within the limits of the projection of the XZ or YZ plane. It may have negative or zero
584 axis position, but its two planar coords must be smaller than the grid size.

585 Direction angles are no longer necessarily constant throughout the calculation: for
586 the focused beam case, each LOS is drawn with a different set of azimuth (ϕ_1) and
587 elevation (ϕ_2) angles. Angles are calculated using the lines that connect the focal point
588 and the imaging screen point, which is the target point for the LOS.

589 The LOS then begins from the focal point, if it resides on the grid side, or from
590 the LOS entry point, calced suitably (here recent relevant calc, upgrade of bversion
591 2.10). From then on, it advances using aiming algos, trying to pass through the targeted
592 screen point. It normally gets the target, or misses it closely! In general, the higher the
593 resolution, the better the accuracy in this respect.

594 For GR pseudo-Newtonian simulations, a logical next step is to introduce $D(\phi_1)$,
595 $D(\phi_2)$, i.e. alter angles along a LOS, from cell to cell, according to the effect of the
596 potential.

597 Then, jet production may be imaged, if the hydrocode can employ external forces
598 from a Kerr BHole.

599 8.1.1. Back in time integration along the LOS

600 In this version, calculations may be done either ahead in time, or backwards in
601 time, from a selected time instant (t_{picked}) backwards. For camera obscura, back in
602 time is generally the correct way to proceed. For radiograph, ahead in time also works
603 fine, assuming a suitable fiducial setup of the jet system vs the observer. t_{picked} is only
604 employed when back in time switch is activated in the external param file. t_{picked} must
605 be generally towards the end of the pre-selected range of dump files, or timeshots, to be
606 loaded to RAM. Sufficient backwards time range must be provided, for the LOS to travel
607 back through time without reaching the beginning of the gris. Else, code cannot finish
608 integration along LOS. When testing, the facility of altering light speed, from rlos1, may
609 be used to play and study this effect.

610 Pathfinding algos have been upgraded for this version. For each combination of XZ
611 or YZ and radiograph or camera obscura, a certain set of such pathfinders are employed.

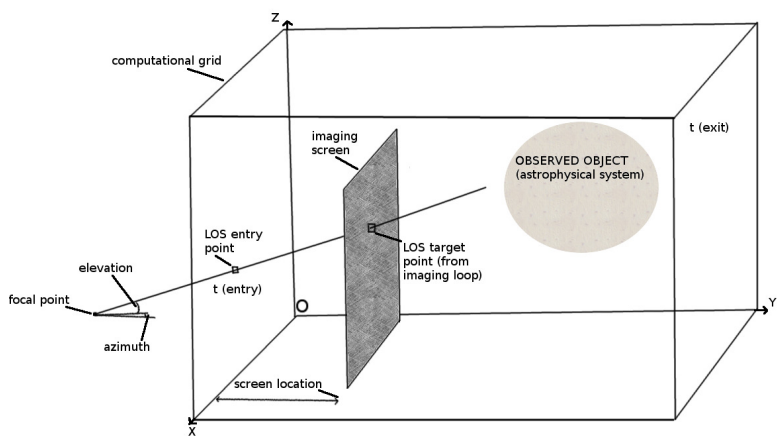


Figure 21. The geometry of focused beam imaging in rlos. A fiducial screen is where the image is formed.

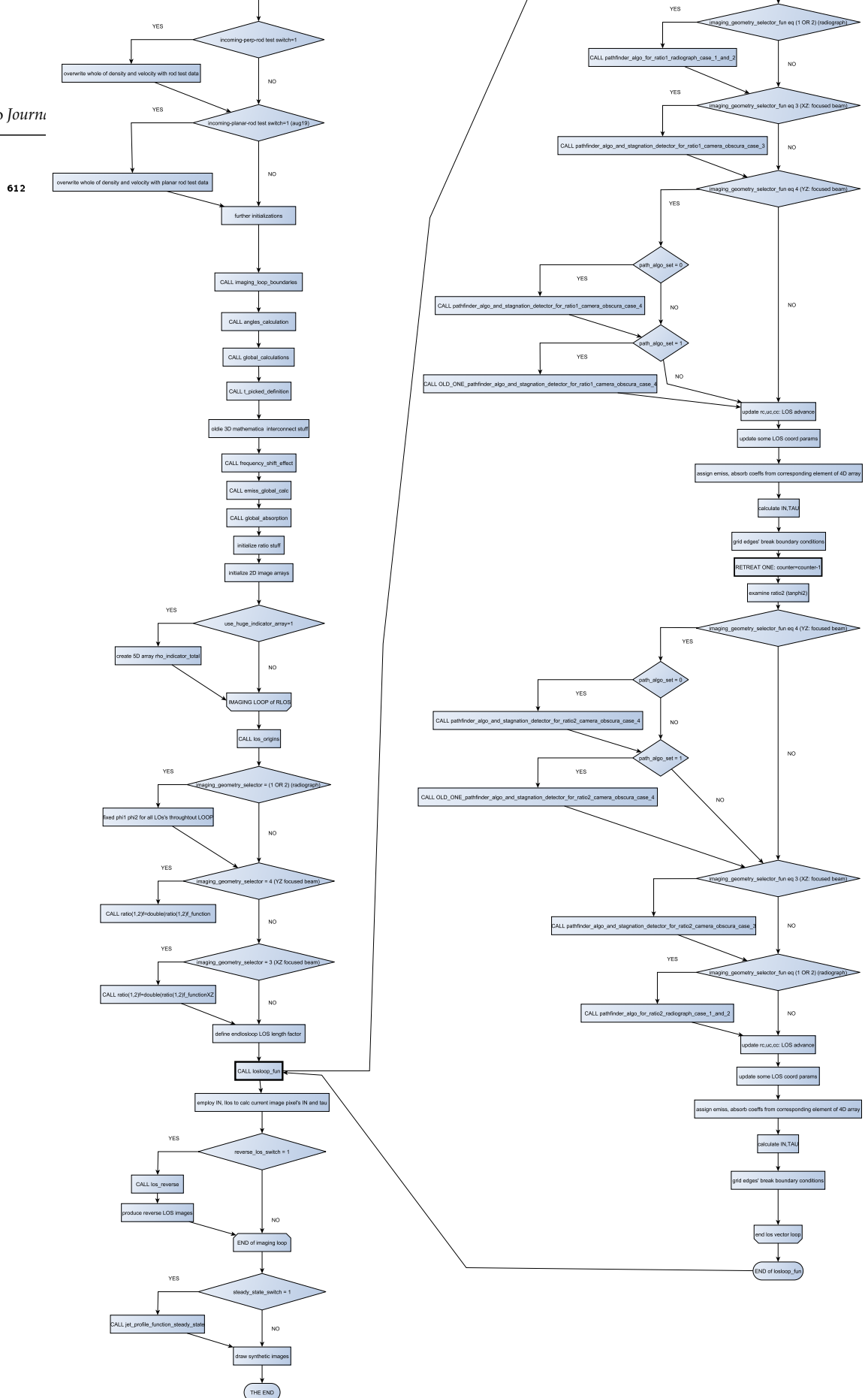


Figure 22. A flow diagram of rlos2.1, depicting the procedures and functions called during program execution.

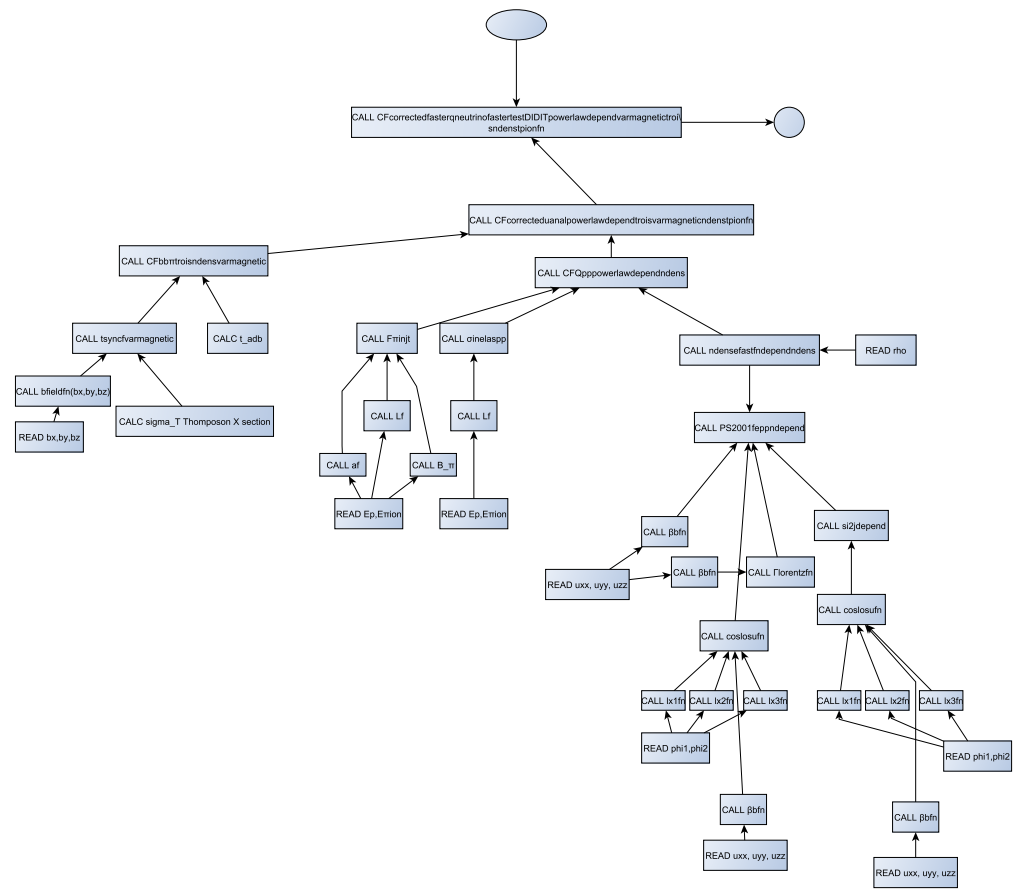


Figure 23. A flow diagram of nemiss, depicting the basic structure of the program.

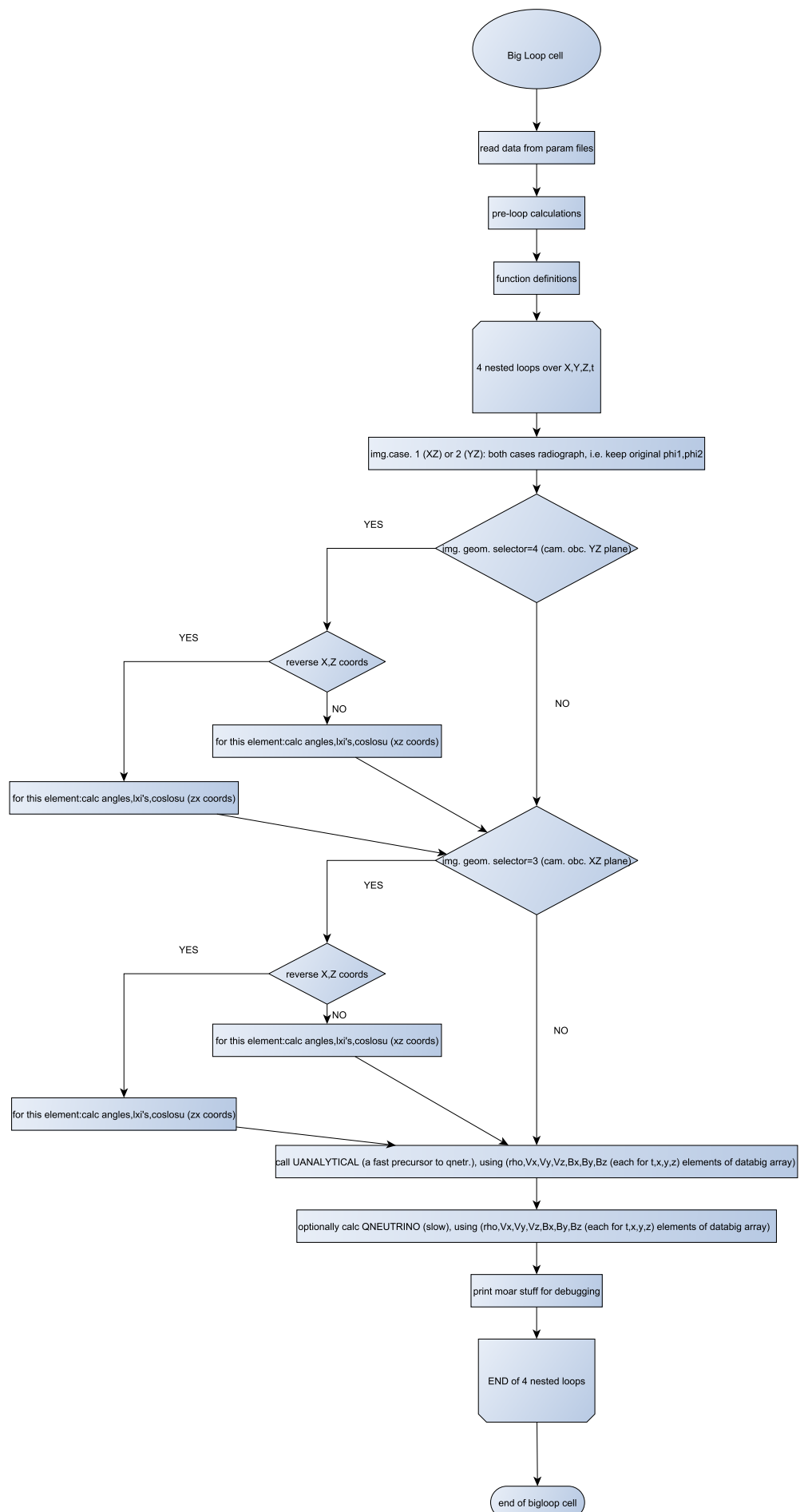


Figure 24. A flow diagram of the main loop of nemiss, where the calculation takes place. This has now been upgraded to 5D, with the addition of a loop for particle energy.

